Master's thesis

Master's Programme in Materials Research

Study Track of Inorganic Materials Chemistry

Hybrid Photocatalysts with Earth-Abundant Plasmonic Materials

Vilma Heczko

2021

Supervisor:
Prof. Pedro Camargo

Examiners:
Prof. Pedro Camargo
University Lecturer Miia Mäntymäki

University of Helsinki
Faculty of Science

HELSINGIN YLIOPISTO
HELSINGFORS UNIVERSITET
UNIVERSITY OF HELSINKI

MATEMAATTIS-LUONNONTIETEELLINEN TIEDEKUNTA
MATEMATISK-NATURVETENSKAPLIGA FAKULTETEN
FACULTY OF SCIENCE

Tiedekunta – Fakultet – Faculty	Koulutusohjelma – Utbildningsprogram – Degree programme
Faculty of Science	Master's Programme in Materials Research

Opintosuunta – Studieinrikting – Study track

Inorganic Materials Chemistry

Tekijä – Författare – Author

Vilma Heczko

Työn nimi – Arbetets titel – Title

Hybrid Photocatalysts with Earth-Abundant Plasmonic Materials

Työn laji – Arbetets art – Level	Aika – Datum – Month and year	Sivumäärä – Sidoantal – Number of pages
Master's thesis	April 2021	58+14

Tiivistelmä – Referat – Abstract

Plasmonic catalysis utilises light energy to drive chemical reactions. Compared to conventional catalytic processes, which are run by high temperatures and pressures, light-driven processes can lower energy consumption and increase selectivity. Conventional plasmonic nanoparticles (Ag, Au) are relatively scarce and expensive, and therefore the use of materials with earth-abundant elements in plasmonic catalysis is widely pursued. Despite their good optical properties, plasmonic nanoparticles are often unsuitable catalysts. Hybrid catalysts, structures consisting of a light-harvesting plasmonic part and a catalytical centre of different material, have emerged as an opportunity to address these challenges and obtain desired properties. This thesis consists of two parts: In the first part, properties of plasmonic materials are described, and previous studies of hybrid catalysts with earth-abundant plasmonic materials are reviewed. Experimental work on plasmonic-catalytic nanohybrids, with TiN as the plasmonic part and Pd as the catalytic entity, is described in the second part. In this context, a Pd/TiN (Pd nanoparticles supported into TiN) catalyst was synthesised, characterised and applied to test catalytical reactions. Contrary to the hypothesis, light-induced rate enhancement was not observed in our current catalytical studies. These results call for further optimisation of synthesis and reaction conditions to prepare an earth-abundant, light-active catalyst.

Avainsanat – Nyckelord – Keywords

catalysis, nanomaterials

Säilytyspaikka – Förvaringställe – Where deposited

Helsinki University Library, E-thesis

Muita tietoja – Övriga uppgifter – Additional information

Contents

List of abbreviations

DFT	Density functional theory
DRM	Dry reforming of methane
DRS	Diffuse reflectance spectroscopy
EDS	Energy-dispersive X-ray spectroscopy
GC	Gas chromatography
HRTEM	High-resolution transmission electron microscopy
LSPR	Localised surface plasmon resonance
MP AES	Microwave plasma atomic emission spectrometry
NIR	Near infrared
NP	Nanoparticle
SEM	Scanning electron microscopy
TEM	Transmission electron microscopy
UV-Vis	UV-Vis spectrophotometry
XRD	X-ray diffraction

1. Introduction

Current chemical processes applied in the chemical industry are energy-consuming, demanding high temperatures and pressures to drive them. New ways of introducing energy to the system would lower energy consumption and allow more precise control of chemical reactions.[1] Catalysis is a cornerstone of the chemical industry, and therefore increased efficiency in these processes significantly impacts the overall consumption of energy and other resources[2].

One of the suggested methods to reach this goal is plasmonic catalysis. This method takes advantage of localised surface plasmon resonance (LSPR), collective oscillation of charge carriers in nanostructures of a suitable conducting material. Thus, energy from the light can be concentrated in small structures and used to drive chemical transformations.[3] The unique optical features of metal nanoparticles have been utilised in glass-making already by Romans and first described scientifically by Faraday in 1857[4,5]. However, their utility in catalysis has been shown less than 20 years ago[6,7].

Commonly used plasmonic materials are gold (Au) and silver (Ag). Recently, interest has grown in utilising other, widely available elements for materials in plasmonic applications.[8,9] Besides being more abundant, these materials permit new advantages in cost, stability and ways to tune the properties.[9,10] However, plasmonic materials are limited in their catalytic properties. Combining two parts, one with plasmonic properties and another with catalytical activity, has been studied to overcome this challenge.[11] In this work, these catalysts are referred to as **hybrid plasmonic catalysts**. For clarity, these hybrid catalysts referred to in this work are denoted as C/P, where C is primarily catalytically active part, and P is the primarily plasmonic part. This notation might be different from the original published works.

In the literature review part of the thesis, some fundamentals of heterogeneous catalysis, plasmonic phenomena and plasmonic catalysis are covered. Then, photocatalysts with earth-abundant materials are reviewed, ordered in sub-sections according to the plasmonic material. In the experimental part, a study of palladium decorated titanium

nitride (Pd/TiN) catalyst is described. The work includes synthesis, characterisation and studies on the catalytical activity of the synthesised catalyst. Chemical reactions employed as model transformations in this work were phenylacetylene hydrogenation and ammonium borane dehydrogenation. The experimental work was conducted between June-December 2020 as a part of the group led by Professor Pedro Camargo at the Department of Chemistry at the University of Helsinki.

2. Literature review

2.1. Heterogeneous catalysis

The International Union of Pure and Applied Chemistry (IUPAC) defines the catalyst as "a substance that increases the rate of a reaction without modifying the overall standard Gibbs energy change in the reaction" and does not change in the reaction[12]. A typical figure, often given in textbooks, is that over 80 % of chemical processes take advantage of catalysis at some point in the process.[2,13] Catalysis plays an essential role in many industries, including food, chemicals, pharmaceutical and fuel production[2].

Typically, catalysis is divided into two branches: in homogenous catalysis, the catalyst is in the same phase as the reaction. In heterogeneous catalysis, the catalyst is in a different phase compared to the reactants and products.[12] Heterogeneously catalysed chemical reaction proceeds via the adsorption of one or more species on the catalyst surface. Adsorption causes activation and a preferential pathway for the reaction that lowers the activation energy of the reaction step.[14] The catalytic activity of a given structure is dependent of the available binding sites and crystal facets as well as electronical properties of the material[13]. An advantage of heterogeneous catalysis that makes it preferred in the industry is the easy removal of catalyst from the reaction products[15]. However, changes in catalyst structure over time, such as sintering, decrease the catalyst activity and selectivity[14].

2.2. Environmental considerations

Catalysis has been recognised as a useful tool for green and environmental chemistry[16,17]. Plasmonic catalysis with earth-abundant materials contribute with many aspects to the more sustainable design of chemical processes. In this section, these aspects are reviewed, reflecting loosely on the 12 green chemistry principles developed by Anastas and Warner.[16]

Plasmonic catalysis can improve selectivity and lower the overall amount of waste of the chemical reaction, and mitigate the formation of harmful by-products[18,19]. New pathways for the reaction can be possible compared to common catalytic systems. Utilising light can lower the temperature needed for the reaction and lower energy consumption.[1] The use of sunlight to power the reaction would decrease the dependence on other, possibly limited energy sources[20].

Nano-sized catalytical structures lower the used amount and increase the effectiveness of the used material[21]. Solid catalysts are easy to separate from the liquid or gaseous reaction[21,22] and are ideally reusable. Studies of catalyst recycling and long-time stability are often included in research on catalysts[23,24]. Ideally, lower reaction temperatures used in plasmonic catalysis can increase the long-time stability of the catalyst and decrease sintering[25]. Long-term stability of catalysts is advantageous for lower consumption of the materials[22], leading to economic and environmental efficiency.

Resources of metals on earth are limited, and for sustainable use of the resources, abundant materials should be preferred relative to scarce ones[16,22]. However, a scarcity of a particular metal is not straightforward. It depends on if the consideration is based purely on the abundance of the metal in the earth's crust, so-called absolute scarcity, or considered together with other factors that can cause changes in the metal availability in the future. These factors include current and expected extraction rates as well as geopolitical, economic, and environmental considerations.[26–28] However, a deep understanding and examining these factors is not in the scope of this work. Instead, different alternatives for typical plasmonic materials Au and Ag are widely acknowledged.

Many applications in catalysis utilise precious metals, and entirely avoiding their use is not reasonable. Scarce elements should be used sustainably, focusing on minimising the use and maximising the recovery.[22]

Photocatalysis is envisaged to greatly impact the sustainable development to a carbon-neutral future. Importance has been given to transferring energy from solar light to chemical energy and applications such as CO_2 reduction to value-added products, splitting water into hydrogen and oxygen and pollution mitigation.[15,29]

2.3. Plasmonic catalysis

2.3.1. Fundamentals of plasmonic phenomena of metal nanoparticles

Interaction of electromagnetic radiation with nanosized material of metallic behaviour causes collective oscillation of the electrons in the material at a resonant frequency. This oscillation enhances absorption and scattering cross-sections of the material, leading to the concentration of light energy in the nanoparticle, increasing the electric field in the vicinity of the particle surface. This phenomenon, observed for structures of smaller dimensions than the incident light wavelength, is called localised surface plasmon resonance (LSPR)[1]. Surface plasmons relax through radiative scattering or non-radiative absorption. The latter leads to the formation of high-energy charge carriers, electrons and holes. After that, energy is quickly dissipated by localised heating in the surroundings. [1,30]

Charge carriers can be excited via two main mechanisms: Intraband transitions are s-to-s transitions that have a low rate, compared to interband d-to-s transitions with a higher rate constant (Figure 1). However, in contrast to intraband transitions, d-to-s transitions are available only at limited irradiation wavelengths, dependent on the energy of d-states of the material.[1,31,32] Exited charge carriers are often called “hot” because their energy is higher than their thermally excited counterparts[3].

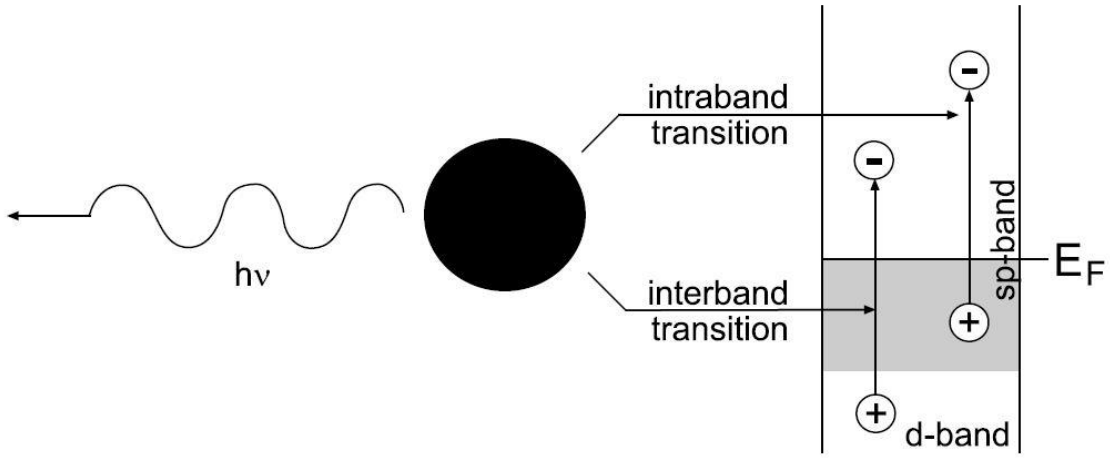

Figure 1. Decay pathways of LSPR excitation. Left: radiative scattering. Right: interband and intraband transitions. Reproduced with permission from Maier, S. A. Localized Surface Plasmons. In Plasmonics: Fundamentals and Applications; Springer US: New York, NY, 2007; pp 65–88. Copyright 2007 Springer Nature.

The optical response of a material is governed by its dielectric properties, described by the complex dielectric function [$\varepsilon(\omega)$]:

$$\varepsilon(\omega) = \varepsilon_r(\omega) + i\varepsilon_i(\omega) \quad (1)$$

Where ω is the frequency of the incident light.[3] $\varepsilon_r(\omega)$ is the real part of the dielectric function, describing the polarisability of the metal, whereas imaginary part $\varepsilon_i(\omega)$ describes the contribution of the absorption in the total extinction of light irradiation, that includes both absorption and scattering[1,31,33]. ε_i is high for metals in wavelengths where d-to-s transitions are accessible, where the absorption is high due to the high rate of this transition[1,32]. Strong resonances can be observed when the real part is negative and the imaginary part is small[34,35]. Typically, plasmonic materials have d-band far from the Fermi level.[1,11] Real and imaginary parts can be expressed as follows:

$$\varepsilon_r = \varepsilon_\infty - \frac{{\omega_p}^2}{\omega^2+\gamma^2} \quad (2)$$

$$\varepsilon_i = \frac{{\omega_p}^2\gamma}{\omega(\omega+\gamma^2)} \quad (3)$$

Where ε_∞ is high-frequency dielectric constant, ω_p plasma frequency and γ damping factor, which can be explained to describe the scattering of free carriers. Free carrier concentration is connected to dielectric function by the function of plasma frequency:

$$\omega_p = \sqrt{\frac{ne^2}{m_e\varepsilon_0}} \quad (4)$$

Where *n* is the free carrier concentration, *e* free carrier charge, m_e the effective mass of the free carrier and ε_0 the dielectric constant of free space.[36]

The resonant light frequency, and therefore the wavelength of maximum absorption, is governed by the electronic structure as well as absorption and scattering cross-sections. The absorption in metal particles can be tuned with the size, shape and surface morphology of the particles, and it is also dependent on the dielectric properties of the surrounding medium.[3] Studies have focused on Ag and Au as plasmonic nanoparticles due to their suitable dielectric properties that enable LSPR excitation in the visible range as well as facile and well-studied colloidal synthesis methods[10]. For many metals, among other Mg, Al, Ga, In, Tl, Sn, Pt, and Pd, LSPR frequency lies in the UV region because of their high plasma frequency[10,35,37]. However, usually for photocatalytic applications absorption in the visible region is interesting, as it includes a more prominent part of the solar radiation[20].

2.3.2. Plasmonic properties of non-metals

In addition to metals, various other materials can support LSPR excitation. For most semiconductor plasmonic materials, ε_∞ in equation (2) can be assumed constant, and Drude-Lorentz model described in 2.3.1 can be used with tolerable accuracy[38]. Plasma frequency links the free carrier concentration of the material to the dielectric constant [equations (2)-(4)]. Availability of free carriers is crucial in the plasmonic properties of a material and govern the energy of LSPR absorption, where higher free carrier concentration relates to the LSPR frequency of higher energy and, therefore, smaller wavelength. High doping of semiconductors is needed to reach high enough free carrier concentration and therefore wavelengths in the visible or near-infrared (NIR) region. Dopants can cause changes in band structure in the material and force hybridisation or distortion of the lattice.[38,39]

A review paper by Agrawal et al. recognises three types of doping of plasmonic semiconductors: Aliovalent, where a lattice atom is replaced with a heteroatom; vacancy doping, formation of either cation or anion vacancies in the material; and last, extrinsic interstitial doping, the inclusion of heteroatom into the space between the lattice atoms. A special feature of doped semiconductor plasmonics is the property of possible dynamical tuning of the LSPR frequency after fabrication.[38] Classes of materials with plasmonic properties with some examples is presented in Figure 2. An example of the effect of doping can be observed by comparing the density of states of two materials. Figure 3 depicts the density of states modelled with density functional theory (DFT) of stoichiometric MoO_3 and hydrogen intercalated $H_{1.68}MoO_3$. In stoichiometric oxide, a bandgap is clear in the absence of states around 1 eV. In the doped oxide, states are continuous from the valence band to the conduction band.[40]

Alternative plasmonic materials can have advantages that are often application-specific. For example, TiN is suggested to be suitable for high-temperature applications because of its high melting point, whereas $Cu_{2-x}S$ containing catalyst has shown prominent rate enhancement with 1500 nm radiation, which is significantly higher than typically observed

with metals[24,41]. Silver suffers from chemical instability, leading to oxidation and mitigation of its strong optical properties, whereas gold is expensive[9,42]. Utilising other plasmonic material can lead to higher thermal and chemical stability as well as lower cost, easier tunability and resonant frequencies more suitable for the application.[9,10]

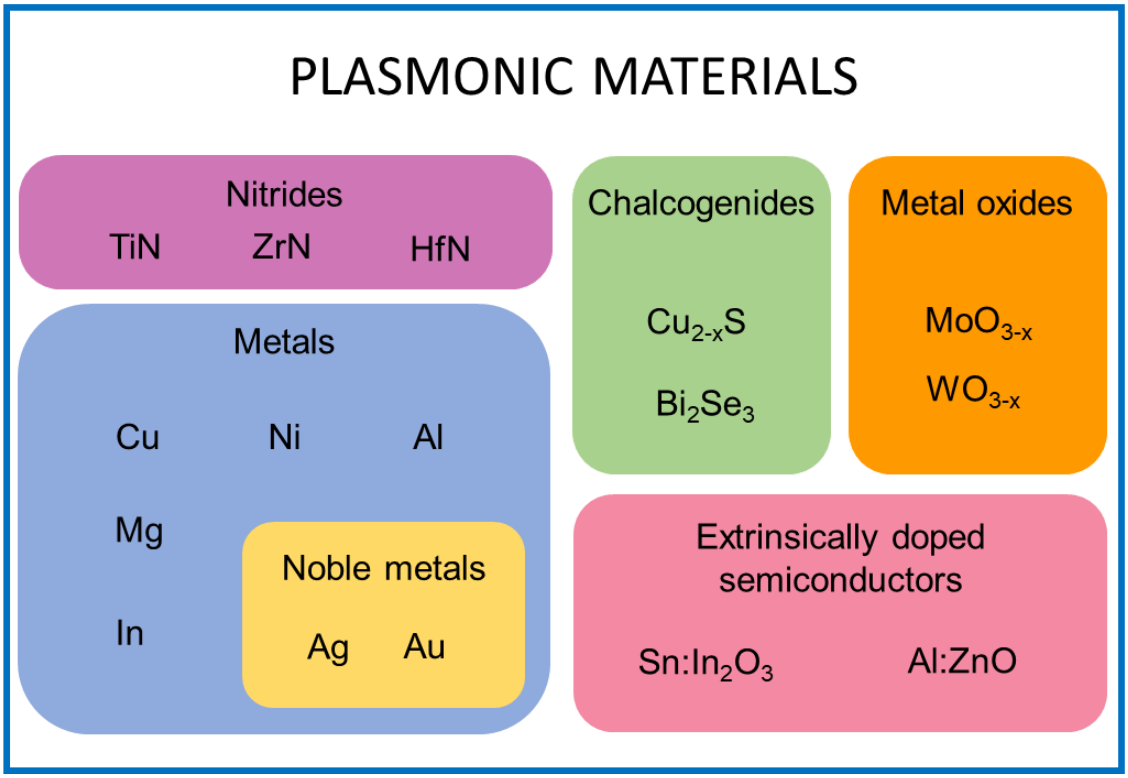

Figure 2. Main classes of plasmonic materials, including examples of each class[3,10,36]. Redrawn and modified from Kim et al.[10]

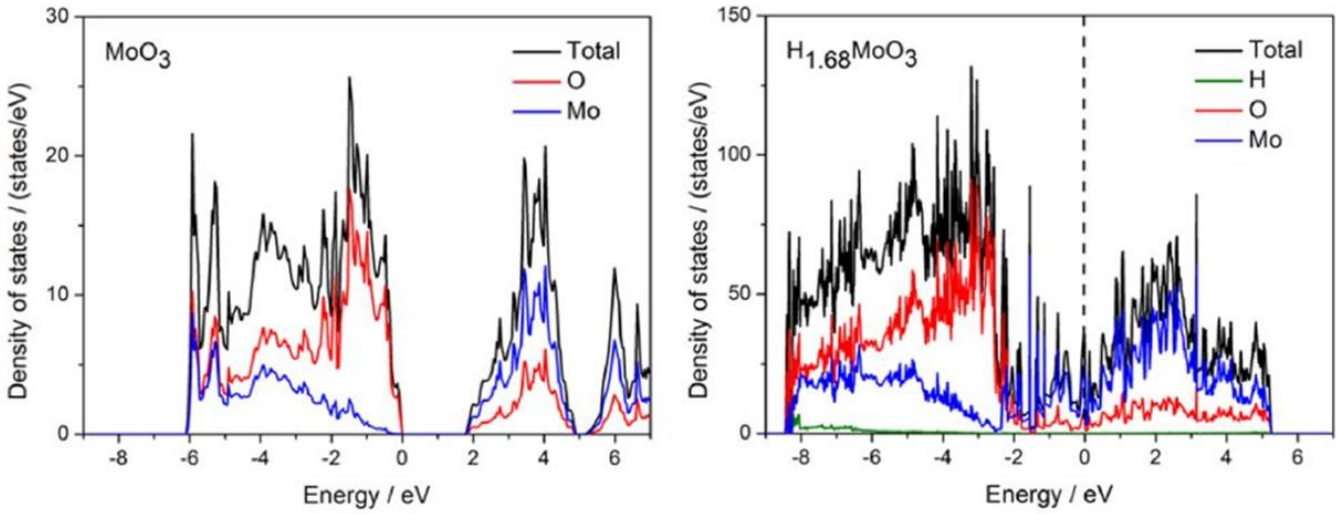

Figure 3. DFT modelled density of states for stoichiometric MoO_3 and $H_{1.68}MoO_3$. Reprinted with permission from Cheng, H.; Wen, M.; Ma, X.; Kuwahara, Y.; Mori, K.; Dai, Y.; Huang, B.; Yamashita, H. Hydrogen Doped Metal Oxide Semiconductors with Exceptional and Tunable Localized Surface Plasmon Resonances. J. Am. Chem. Soc. ***2016****, 138 (29), 9316–9324.. Copyright 2016 American Chemical Society.*

2.3.3. Plasmonic materials for catalysis

Nanostructures with plasmonic properties have been reported to enhance a vast amount of chemical reactions under light irradiation. Typically, these enhancements have been explained by hot-carrier mediated mechanism, termed indirect excitation. In this mechanism, the reaction is catalysed by the formation of hot charge carriers in the plasmonic material that are subsequently transferred to the adsorbing molecule.[1] (Figure 4, A)

Adsorption of the molecule on the nanoparticle surface can lead to the formation of hybridised nanoparticle-adsorbant states. Upon decay of LSPR in the nanoparticle, coupling of plasmon and these states can lead to formation of hot electrons in the nanoparticle-adsorbant states. This mechanism is called direct transfer, or chemical interface damping. [20,43] (Figure 4, B)

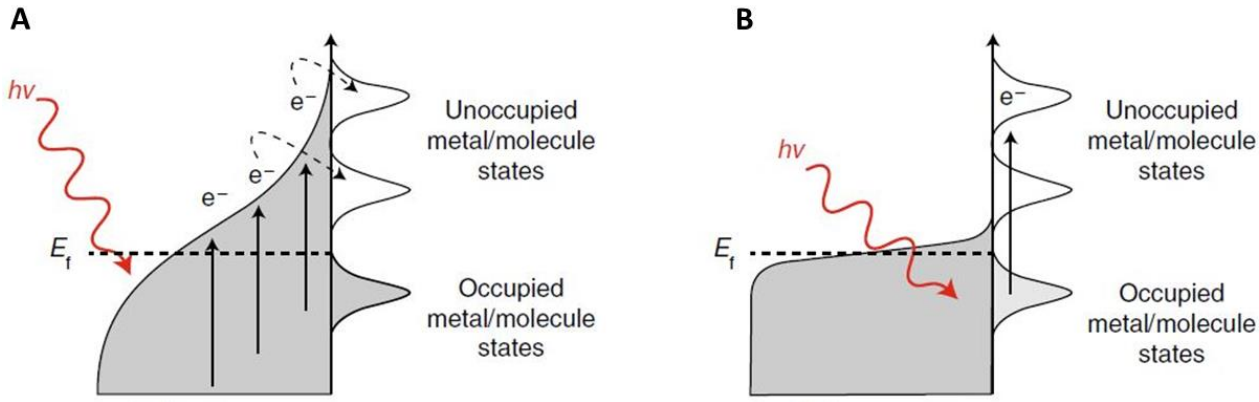

Figure 4. Energy transfer mechanism at plasmonic catalyst/molecule adsorbate interface. A: Indirect energy transfer, B: Direct energy transfer. Reprinted with permission from Aslam, U.; Rao, V. G.; Chavez, S.; Linic, S. Catalytic Conversion of Solar to Chemical Energy on Plasmonic Metal Nanostructures. Nat. Catal. ***2018****, 1 (9), 656–665 Copyright 2018 Springer Nature*

Also photothermal effect, heat formed from the dissipation of the LSPR excitation can drive a chemical process[44,45]. Heating can be localised in a small volume and cause a temperature increase of several hundreds of degrees, avoiding unwanted heating of the surroundings[44–46]. Among other applications, photothermal properties of nanostructures have been applied in plasmon-assisted chemical vapour deposition[46], photothermal cancer therapy[47,48] and water distillation[49].

Different modes of enhancement are challenging to distinguish. Discerning the different modes of enhancement in proposed systems is a significant part of the research on plasmonic catalysis. The degree of thermal effects in the system has been studied and discussed in the research community, with some publications questioning the significance of the non-thermal effects to the rate enhancement.[50,51] According to Baffou et al.[51], suitable methods for differentiating the thermal and non-thermal effects include studies of the reaction rate at different illumination intensities, wavelengths, beam diameter or polarisation. Also, precise temperature measurements of the system, with, for example, infrared camera, could be used.

2.4. Hybrid plasmonic catalysts

Despite the advances achieved in plasmonic catalysis, the catalytical activity of used plasmonic nanoparticles is limited. Combining plasmonic material with a catalytically active component has emerged as a new possible pathway of development for photocatalysts. This possibility leads to vast opportunities to tune the system for the precise needs in question.[11]

Transition metals are widely used in heterogeneous catalysis and can also be incorporated into hybrid systems as catalytic part. Transition metals have a d-band close to Fermi level, making them unsuitable for plasmonic applications in visible wavelengths. However, the proximity of Fermi level leads to stronger adsorption properties that are favourable in catalytic metal.[11,52]

In “traditional” semiconductor-based heterogeneous photocatalysis, an electron-hole pair is excited with radiation of energy as high or higher than the bandgap of the material. The formed electrons and holes can then participate in oxidation and reduction reactions on the catalyst surface.[29] For many materials, for example, the typically used TiO_2, this can be archived only in the UV region. Because this region contributes little to the total intensity of solar irradiation, a considerable amount of research has been focusing on shifting the applicable region to the visible.[53] One of the strategies is to incorporate plasmonic structures into the semiconductor[6]. Some examples of this approach utilising earth-abundant plasmonic materials are described in the following sections.

Antenna-reactor photocatalyst is a term used in some of the literature on hybrid plasmonic structures and describes well the working principle. It was coined in 2016, with pioneering work on Pd/Al catalysts for hydrogen dissociation and acetylene reduction. (See section Aluminium). Here “antenna” refers to the plasmonic part: it concentrates the energy from incoming wave to a small volume, similarly as radio-antennas work[54], and transfers it to the reactor, the catalytic part, that provides the preferred site for the reaction to take place.[55,56] Hybrid structures can have different morphologies, depicted in Figure 5. For

the functioning of the catalyst, important is the type of contact - or lack of it - that governs the coupling effects between the two parts.[11,57]

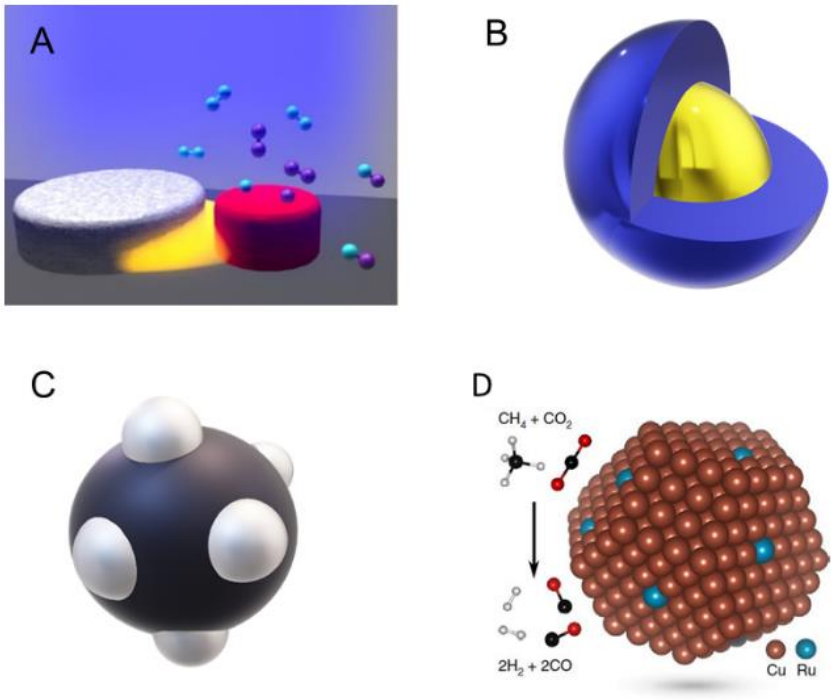

Figure 5. Schematic models of distinct structures of hybrid plasmonic catalysts. A: Catalytic dimer, where plasmonic and catalytic parts are separated. B: Core-shell structure C: Plasmonic particle with catalytic islands. D: Alloyed catalyst. A: Reprinted with permission from Zhang, C.; Zhao, H.; Zhou, L.; Schlather, A. E.; Dong, L.; McClain, M. J.; Swearer, D. F.; Nordlander, P.; Halas, N. J. Al-Pd Nanodisk Heterodimers as Antenna-Reactor Photocatalysts. Nano Lett. ***2016****, 16 (10), 6677–6682. Copyright 2016 American Chemical Society. D: Reprinted by permission from Zhou, L.; Martirez, J. M. P.; Finzel, J.; Zhang, C.; Swearer, D. F.; Tian, S.; Robatjazi, H.; Lou, M.; Dong, L.; Henderson, L.; Christopher, P.; Carter, E. A.; Nordlander, P.; Halas, N. J. Light-Driven Methane Dry Reforming with Single Atomic Site Antenna-Reactor Plasmonic Photocatalysts. Nat. Energy* ***2020****, 5 (1), 61–70 Copyright 2020 Springer Nature*

Electronic fields formed by the LSPR excitation can enhance the absorption in the catalytic material, even if the parts are not in contact[56]. (Figure 5, A) In these structures enhancement of electromagnetic fields is the driving force for the increased catalytic rate. In their review, Araujo and colleagues suggest careful consideration of designing these binary structures. The authors point out that the shape and size of the plasmonic entity, as well as hybridisation between plasmonic particles and catalytic-plasmonic particle

distance, should be optimised to take advantage of the strongest areas of enhancement in the formed electromagnetic fields.[57]

Electronic coupling involves charge transfer between materials in contact[11].(Figure 5, B and C) Coverage of catalytic metal on plasmonic nanoparticle can guide the dissipation of LSPR and lead to increased formation of electron-hole pairs instead of scattering compared to monometallic nanoparticle[58]. This effect depends on the electronic properties of both metals. High ε_i for catalytical part and small for the plasmonic part, leads to the most prominent energy transfer.[59] A modification in the decay pathway has also been observed in plasmonic metal–catalytic semiconductor system, where plasmon-induced electric fields caused enhanced absorption in the semiconductor[60]. The difference of plasmon decay in a bare plasmonic nanoparticle (NP) and a core-shell particle is illustrated in the schematic drawing in Figure 6.

Contact of catalytic and plasmonic parts can cause a lowering in the catalyst d-band, changing its catalytical properties, while on the other hand, non-plasmonic metal causes dampening of absorption of the plasmonic metal core. In alloys (Figure 5, D), materials are mixed on the atomic level and form a distinct band structure.[11]

The following sections review some promising earth-abundant materials for plasmonic catalysis and binary plasmonic-catalytic systems utilising these materials. It should be noted that the reviewed studies are focused on photocatalysis; different photoelectrocatalytic systems (for example, ref. 29, 30) utilise the same principles but are not covered in this work.

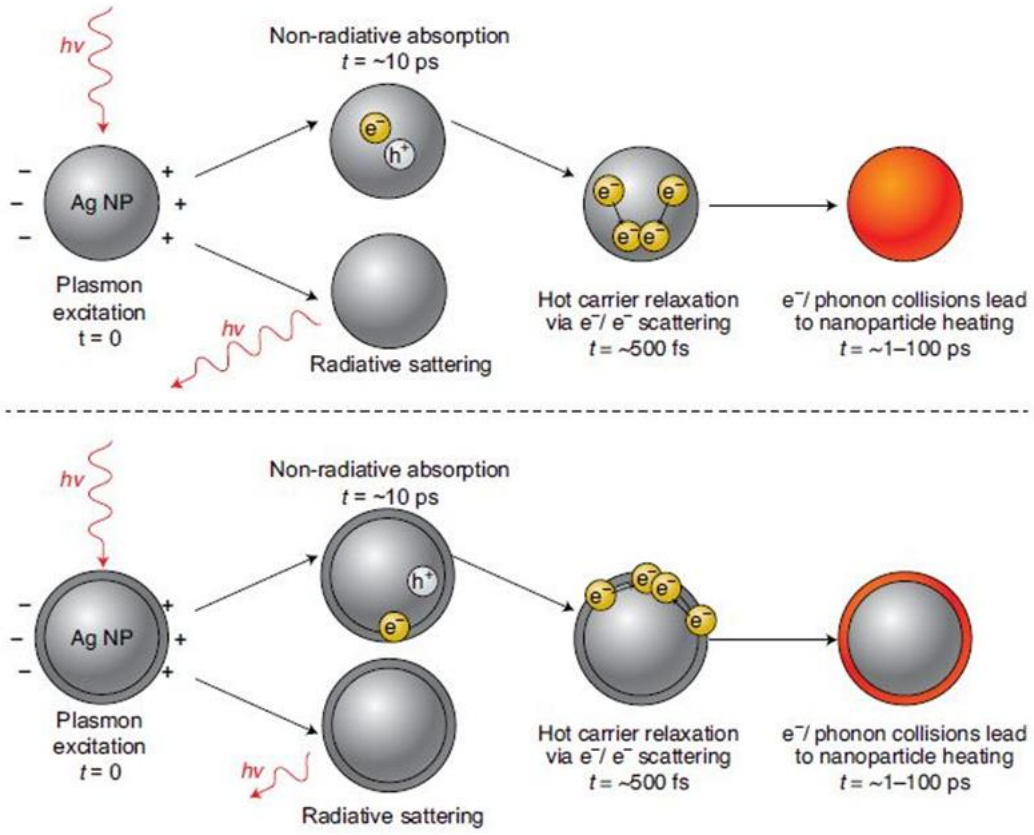

Figure 6. Dissipation of plasmonic excitation in Ag NP and core-shell NP. Reprinted with permission from Linic, S.; Chavez, S.; Elias, R. Flow and Extraction of Energy and Charge Carriers in Hybrid Plasmonic Nanostructures. Nat. Mater. ***2021*** *15 (2), Copyright 2021 Springer Nature*

2.4.1. Copper

With LSPR excitation in the visible range, Cu is usually mentioned alongside Ag and Au as a plasmonic metal[1]. Gawande et al. attribute in their review the interest in the use of Cu NPs in catalysis as alternatives to noble metals in their high natural abundance, low cost and versatile preparation methods[63]. Wet chemical synthesis is popular, due to simple laboratory techniques and good control over the size and shape of the particles. Desired properties of the particles can be attained by reduction from Cu(I) or Cu(II) containing precursors.[63]

However, the use of Cu nanoparticles has been hindered by the chemical instability caused by the easy oxidation of Cu NPs under atmospheric conditions. Oxidation of the particles deteriorates the plasmonic properties. Wet synthesis methods lead to particles

with low crystallinity that are more easily oxidised than crystalline particles formed by gas-phase methods.[64] Disregarding the synthesis method, formed particles must be shielded from oxidation by incorporating them into a substrate or forming core-shell particles.[63,64] Studies have reported harvesting LSPR enhancement for chemical transformations by single-metal Cu systems in, for example, graphene supported Cu NPs for coupling of nitroaromatics[65] and selective epoxidation on Cu NPs[66]. Some binary systems are reviewed in the next section.

Wang et al. studied ZnO/Cu catalyst for methanol synthesis via CO_2 oxidation, attaining 1.5 -fold enhancement of methanol production rate under light irradiation[67]. The catalyst was synthesised by co-precipitation of precursors in ½ ratio of Cu and Zn. The induction of hot electrons was justified by studies of varying light intensity, different irradiation wavelengths (Figure 7) and kinetic isotope effect. The authors report apparent activation energy reduction by 40 % compared to reactions performed in dark.

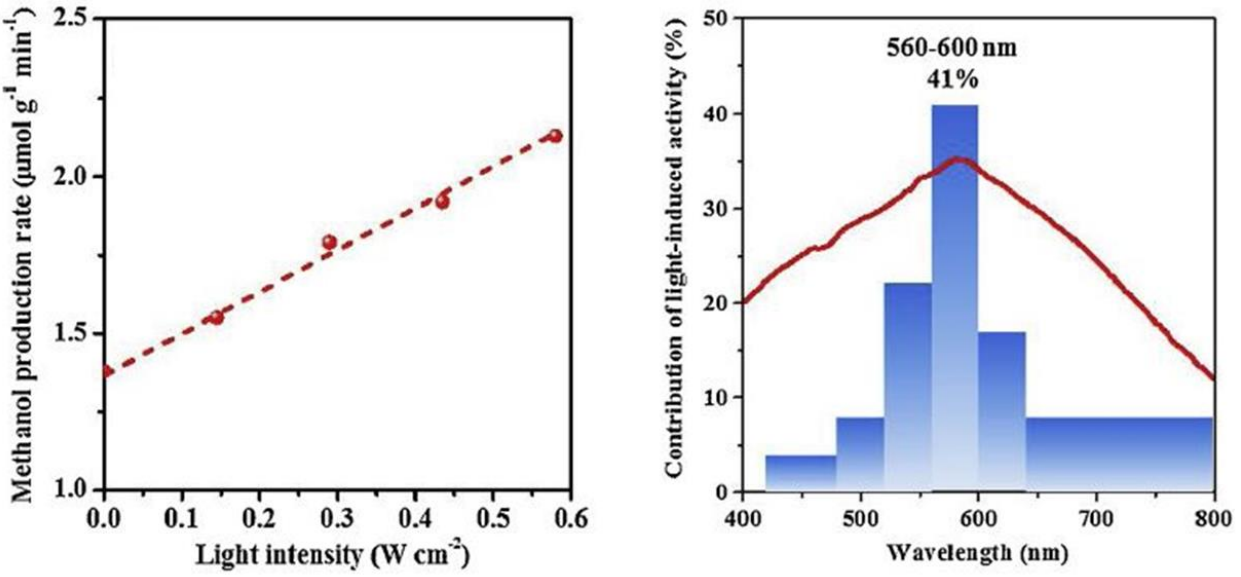

Figure 7. Demonstration of hot electron induced enhancement. Left: reaction rate with varying light intensity, Right: Dependence of reaction rate on the irradiation wavelength. Red line follows the absorption spectra. Reprinted from Wang, Z. jun; Song, H.; Pang, H.; Ning, Y.; Dao, T. D.; Wang, Z.; Chen, H.; Weng, Y.; Fu, Q.; Nagao, T.; Fang, Y.; Ye, J. Photo-Assisted Methanol Synthesis via CO2 Reduction under Ambient Pressure over Plasmonic Cu/ZnO Catalysts. Appl. Catal. B Environ. ***2019****, 250 Copyright 2019, with permission from Elsevier*

In another study, Xu and co-workers combined Cu spheres with catalytical properties of Co or Ni[68]. Cu particles of five different sizes (between 55-440 nm) were synthesised using L-ascorbic acid, and either Co or Ni was reduced on these spheres with sodium borohydride. These catalysts were studied in the hydrogen evolution from ammonium borane at room temperature, where the catalyst containing 150 nm Cu particles with Co delivered the best catalytical activity under light irradiation. In addition to observed light-dependent catalytical activity, charge carrier effects were proven by collecting photogenerated electrons. Notable was the capability of the system to increase the otherwise lower catalytical activity of non-noble Co and Ni in this reaction.

Zhou et al. formed a single-atom catalyst by alloying a small amount of Ru with Cu[23]. In dry reforming of methane (DRM) experiments, single-atom concentration and lower reaction temperature compared to a thermal process increased stability and use-life of the catalyst. This effect was explained by decreased poisoning of the catalytic centres by coke formation. Furthermore, the selectivity increased under light irradiation compared to a thermal process.

2.4.2. Aluminium

Aluminium is, after Si and O, the third most abundant element in the earth's crust[69]. Al has a high plasma frequency and therefore, LSPR frequency in the UV region, where Ag and Au are restricted. Al can be tuned over an extensive range of wavelengths, with LSPR frequency depending on the particle size, shape, and oxidation.[70] (Figure 8) The large extent of the oxidation leads to deterioration of the plasmonic properties.[71] Upon exposure to air, a few nanometres thick passivating oxide layer forms stabilise the Al core to withstand further oxidation[71,72].

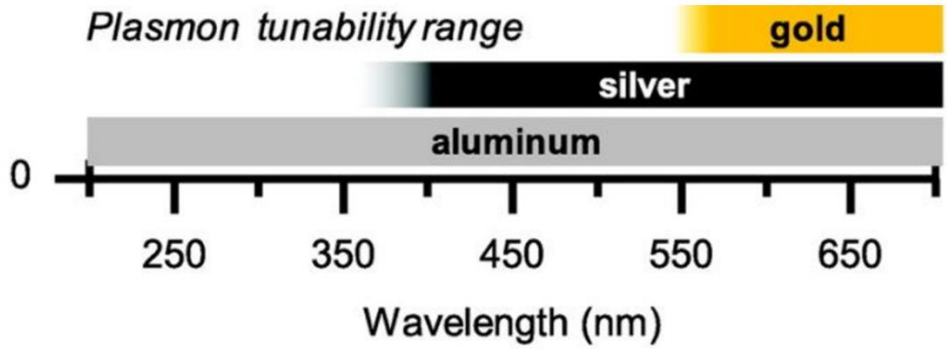

Figure 8. LSPR tunability of aluminium compared to gold and silver. Reprinted with permission from Knight, M. W.; King, N. S.; Liu, L.; Everitt, H. O.; Nordlander, P.; Halas, N. J. Aluminum for Plasmonics. ACS Nano ***2014****, 8 (1), 834–840. Copyright 2014 American Chemical Society*

Lithography[56] and colloidal methods[73–75] have been used to synthesise Al nanoparticles. Impurities can cause polycrystallinity of lithographical particles, whereas precursors used in a colloidal synthesis are reactive with air and water, prohibiting aqueous methods[76]. However, in solvent methods, the particle size can be changed with varying solvent ratios of surface ligands[74,75].

Some of the first work on binary plasmonic-catalytic systems have been performed utilising Al nanocrystals. Halas group showed proof of the binary plasmonic catalyst concept in two morphologically different Pd/Al systems in 2016[55,56]. Both systems showed light enhanced hydrogen dissociation assigned to synergistic functions of both plasmonic and catalytical metals where enhanced local fields formed by Al caused hot carrier formation in the catalytic metal. With Pd decorated Al nanocrystals, selectivity rise in acetylene reduction was observed[55]. Lithographically prepared Pd/Al nanodisk dimers could be used to present the effects of the irradiation wavelength, distance between the plasmonic and catalytic entities and the light polarisation angle on the reaction rate[56].

In the following studies, the system was developed further: For more optimised use of the LSPR effect and the catalytic noble metal, Pd was deposited on the areas of highest local field enhancement, on the edges of a colloidally prepared Al nanoparticle (Figure 9). This preferential growth was reached by the slow addition of the Pd-precursor in the catalyst reduction step of the synthesis[77]. A colloidal Pd/Al system could also be used to lower the

reaction barrier and consequent break C-F bond that is a chemical transformation relevant for environmental and industrial purposes[78].

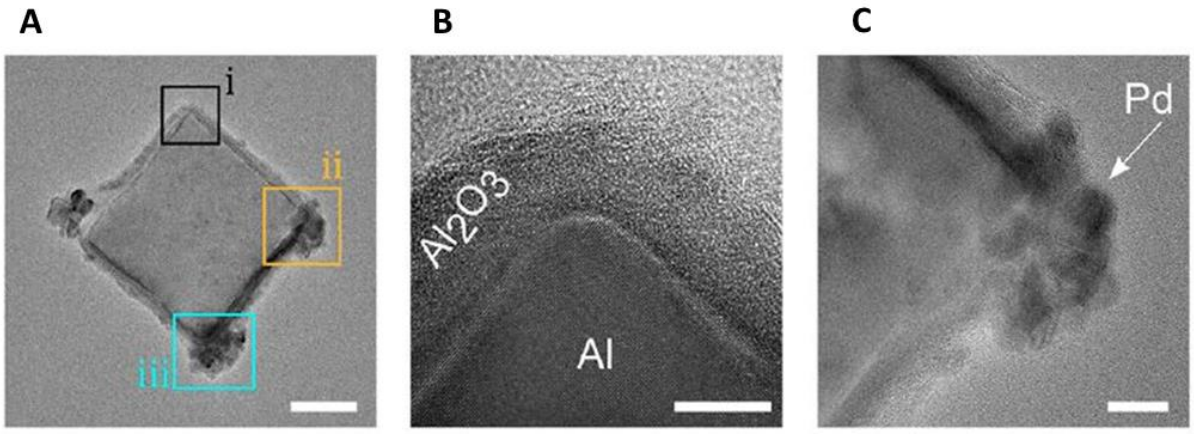

Figure 9. Transmission electron micrographs of Pd/Al with preferential Pd growth on the Al particle corners. A: Al NP with reduced Pd nanoclusters. Scale bar: 50 nm. B: Part I in A. Scale bar: 5 nm. C: Reduced Pd cluster on the corner of Al NP. Scale bar 20 nm. Reprinted with permission from Robatjazi, H.; Lou, M.; Clark, B. D.; Jacobson, C. R.; Swearer, D. F.; Nordlander, P.; Halas, N. J. Site-Selective Nanoreactor Deposition on Photocatalytic Al Nanocubes. Nano Lett. ***2020****, 20 (6), 4550–4557. Copyright 2020 American Chemical Society.*

A noble-metal free CuO/Al catalyst was studied by Robatjazi et al. for reverse water gas shift reaction[79]. A catalyst of core-shell structure of Al core, with a polycrystalline cuprous oxide shell supported on γ-Al_2O_3 was shown to enhance the rate and selectivity of the reaction under light irradiation. Via studying photon flux dependence of the reaction, local temperature, optical absorption and electric field enhancement, the authors concluded the enhancement to be hot-carrier mediated, leading to increased optical absorption in the catalyst semiconductor.

Swearer et al. showed a procedure to reduce multiple different, catalytically relevant metals on Al-nanoparticles by polyol assisted reduction[80]. In the following study, Ir/Al catalyst for transforming greenhouse gas N_2O to N_2 and O_2[19]. Light-induced catalysis led to high selectivity, and no formation of undesirable NO_x species was observed with temperatures lower than used in traditional thermal catalysts. No observation of change in activation energy or influence of the light intensity lead the authors to presume the

enhancement to be driven by photothermal effects and the hot carrier pathway to be hindered due to the limiting step of the reaction, O_2 desorption that is not affected by hot carriers.

The photocatalytic performance of TiO_2 can be enhanced by adding Al crystals to the catalyst structure. Multiple studies have shown increased efficiency of degradation of organic pollutants with different TiO_2/Al-based systems.[81,82]

2.4.3. Magnesium

In recent years, magnesium has gained attention as an abundant metal capable of supporting an LSPR excitation. It is biocompatible, with a plasmonic response tunable from UV to NIR region[34,83]. Mg metal forms a hexagonal closed packed crystal structure that is untypical among plasmonic metals. Compared to metals with face-centred cubic lattices, hexagonal structures have distinct crystal shapes and exposed surfaces[34].

The plasmonic response of Mg can be changed by inducing a phase change by incorporating hydrogen into the crystal structure. Plasmonic Mg can be switched to non-plasmonic MgH_2 by introducing H_2. This change can be reversed by O_2 treatment.[84] This feature can be utilised in novel applications of dynamic plasmonics, for example, display technology[85].

Mg has a high negative reduction potential that causes fast oxidation of Mg NPs. Due to its reactivity, colloidal synthesis of Mg NPs must be performed in a carefully controlled environment with a dry solvent. Formed particles must be protected with an oxide shell to remain stable in air. Well-defined reduction methods developed for Ag and Au NP synthesis are not suitable because of the redox potential.[34,86]

However, this property of ready oxidation can drive galvanic replacement to decorate the Mg particles[86]. Galvanic replacement is an electrochemical process driven by the differences in reduction potentials of the two participating metals. Sacrificial metal, present in solid, oxidises and dissolves and is replaced by metal from solution with higher reduction potential.[87]

Au, Ag, Pd and Fe was reduced on Mg NPs using galvanic replacement in a study conducted by Asselin et al[86]. The authors describe the possibility of stepwise reduction, allowing decorating a particle with multiple metals. Hypothetically, the galvanic replacement could be used to reduce any metal with a higher reduction potential[34]. Plasmonic MgO/Mg structures have enhanced photocatalytic decomposition of FS_6 in a study by Gutierrez and colleagues[83].

2.4.4. Molybdenum oxide

While stoichiometric molybdenum trioxide is an insulator, plasmonic properties can be induced by reducing oxygen or intercalating hydrogen atoms into the layered structure of MoO_3. These structures can be denoted as molybdenum oxide MoO_{3-x} or as hydrogen molybdenum bronzes, respectively.[88,89] LSPR absorption of these materials can be tuned by the extent of the doping, which can be controlled by the reduction temperature. In an H_2 spillover method, chemisorbed H_2 on the surface is dissociated by metal and intercalates into the lattice, causing reduction of the cation and an oxygen vacancy (Figure 10). In the presence of metal, hydrogen is intercalated at lower temperatures. This effect is dependent on the ability of the metal to dissociate hydrogen.[40]

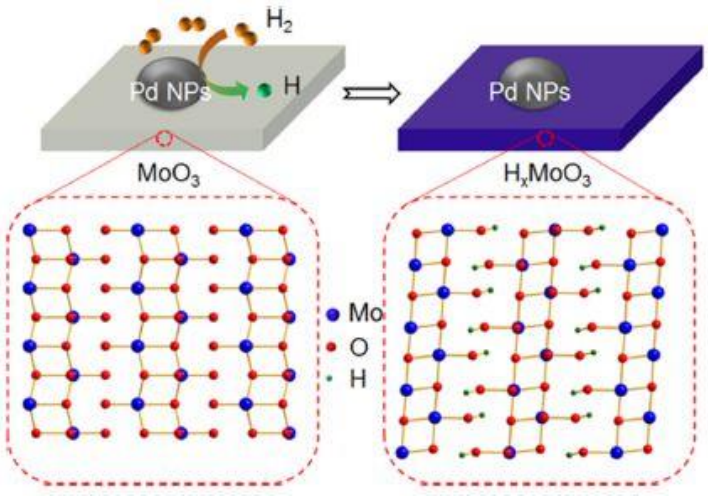

Figure 10. Schematic image of H_2 spillover process on MoO_3 surface. Reprinted with permission from Cheng, H.; Wen, M.; Ma, X.; Kuwahara, Y.; Mori, K.; Dai, Y.; Huang, B.; Yamashita, H. Hydrogen Doped Metal Oxide Semiconductors with Exceptional and Tunable Localized Surface Plasmon Resonances. J. Am. Chem. Soc. 2016, 138 (29), 9316–9324. Copyright 2016 American Chemical Society.

In 2015, Cheng et al. composed a Pd/MoO_{3-x} catalyst[88]. In the synthesis, MoO_3 nanoplates were obtained by thermal decomposition of $(NH_4)_6Mo_7O_{24}$. In the next step, $NaBH_4$ reductant was added to a suspension of H_2PdCl_4 impregnated plates. Reduction with $NaBH_4$ caused impregnated Pd ions to form metallic palladium and Mo atoms to reduce from the oxidation state of 6+ to 5+ and form oxygen vacancies in the oxide. Diffuse reflectance spectroscopy (DRS) measurement showed a rise of an absorption peak for an as-synthesised hybrid at 640 nm, compared to a pure stoichiometric MoO_3. According to X-ray diffraction (XRD) measurement, no phase change occurred during the reduction. The prepared catalyst oxidised, causing red-shift and lowering of the LSPR absorption peak within hours. The absorption, however, could be recovered with $NaBH_4$ treatment. (Figure 11) The catalyst showed plasmon-enhanced catalytic activity for hydrogen formation from ammonium borane and Suzuki–Miyaura coupling reactions.[88]

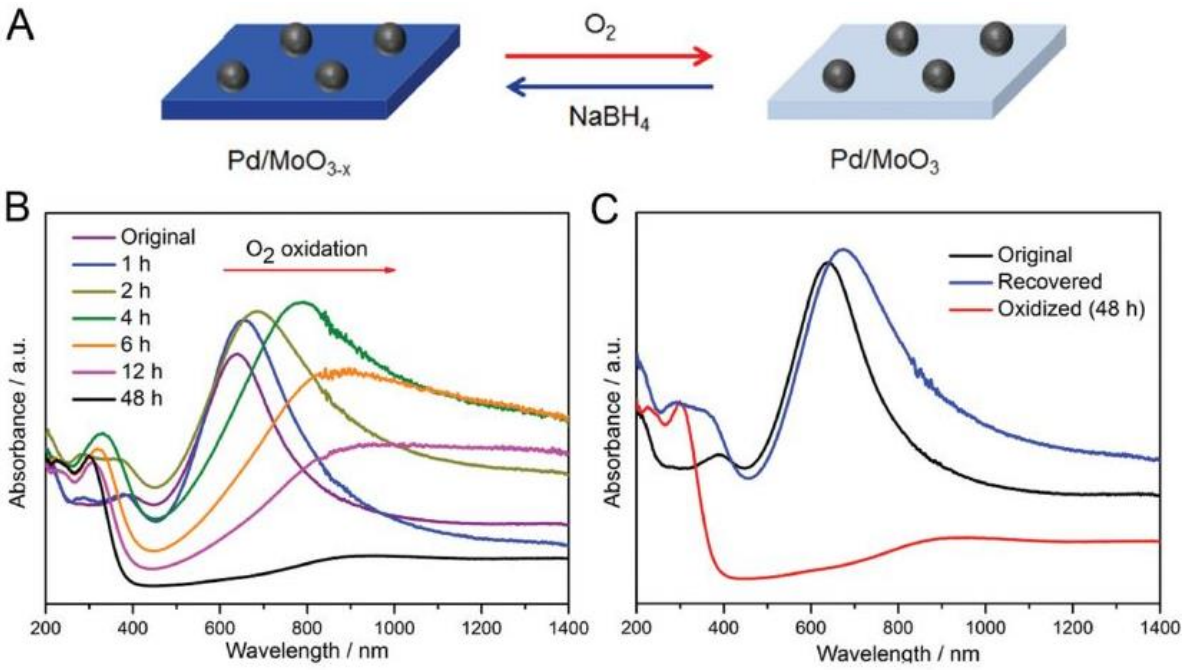

Figure 11. Pd-MoO_{3-x} catalyst. A: Oxidation and reduction of the catalyst. B: DRS spectra of catalyst at different times after synthesis. C: DRS spectra of original, oxidised, and recovered catalyst. Reprinted with permission of John Wiley & Sons - Books, from Cheng, H.; Qian, X.; Kuwahara, Y.; Mori, K.; Yamashita, H. A Plasmonic Molybdenum Oxide Hybrid with Reversible Tunability for Visible-Light-Enhanced Catalytic Reactions. Adv. Mater. ***2015****, 27 (31), 4616–4621; permission conveyed through Copyright Clearance Center, Inc.*

In a different study, Pt/H_xMoO_{3-y} catalysts showed photocatalytic activity for deoxyhydrogenation of sulfoxides, leading to a 2-fold faster reaction than in dark conditions[18]. Interestingly, prepared comparison samples of catalysts, Pt/SiO_2 and Pt/Al_2O_3, showed no reactivity, leading to a conclusion that Pt nanoparticles were not the main active sites of the catalysts. Studies of catalytic activity of Pd H_xMoO_{3-y} and Ru/H_xMoO_{3-y} lead to a conclusion that the metal activates the hydrogen dissociation on the catalyst surface and by that leads to a better yield than pure H_xMoO_{3-y} catalyst. Oxygen vacancies and intercalated hydrogen ions were proposed to be the catalytic reaction sites, based on the stoichiometry of these species determined by thermogravimetrical analysis. The deduced reaction mechanism is presented in Figure 12.

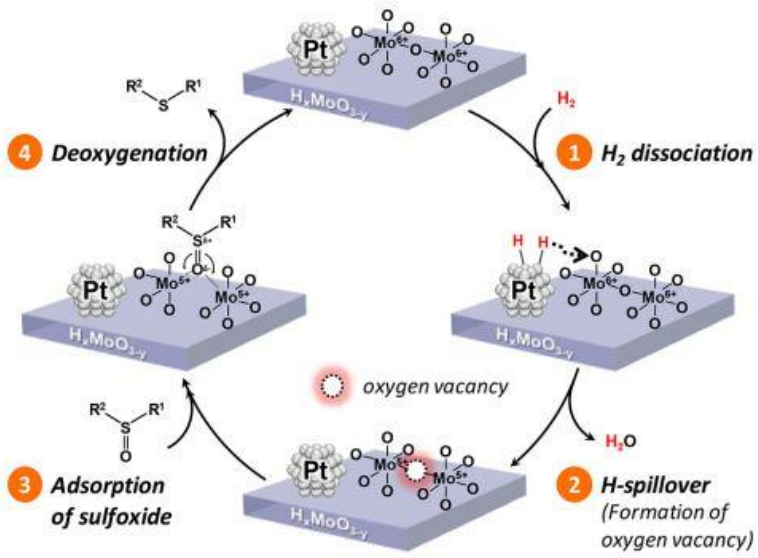

Figure 12. Proposed reaction mechanism of deoxyhydrogenation on Pt/H_xMoO_{3-y} catalysts. Reprinted with permission from Kuwahara, Y.; Yoshimura, Y.; Haematsu, K.; Yamashita, H. Mild Deoxygenation of Sulfoxides over Plasmonic Molybdenum Oxide Hybrid with Dramatic Activity Enhancement under Visible Light. J. Am. Chem. Soc. ***2018****, 140 (29), 9203–9210. Copyright 2018 American Chemical Society*

The hydrogen spillover process was also employed to synthesise a Ru/H_xMoO_{3-y} catalyst by Yin and co-workers[90]. Plasmonic enhancement was observed under light irradiation in p-nitrophenol reduction as a model reaction, describing the Ru NPs as the catalytically active centres of the reaction. In a subsequent study, alloying Pd to Ru to form RuPd/H_xMoO_{3-y} catalyst, the authors showed higher catalytical activity in the same reaction[91].

Zhang et al. utilised plasmonic properties of MoO_2[92]. Solvothermal process, followed by impregnation and calcination, was employed to obtain Pt/MoO_2 core-shell particles. The reaction rate for preferential oxidation for CO was increased under light, and side product formation was decreased compared to dark reaction conditions. The authors explain hot-electron transfer to be the mode of plasmonic enhancement.

2.4.5. Tungsten oxide

Monoclinic WO_{3-x} grows in preferential {010} direction, forming wires or rods with corner and edge-shared WO_6 octahedra[93]. Non-stoichiometric tungsten oxide has been shown to catalyse light-assisted a myriad of chemical reactions using its oxygen vacancies. These reactions include ethanol dehydration to form ethylene[94], CO_2 reduction[93] and hydrogenation of olefins[95].

Lou et al. showed in 2016 that non-stoichiometric WO_{3-x} could be used to drive LSPR enhanced catalytic reaction on external catalytic site attached to the plasmonic material[96]. As a proof-of-concept, Suzuki coupling, which was inactive on WO_{3-x} structures, was shown to have increased catalytic activity on Pd/WO_{3-x} structures under long-wavelength (λ>650 nm) irradiation. WO_{3-x} nanowires were prepared using a solvothermal method from $W(CO)_6$ precursor, and Pd was reduced with $NaBH_4$. The increased rate and selectivity were attributed to the photothermal effects of the catalyst. In further work, Lou and co-workers combined a studied catalyst for ammonium borane dehydrogenation, Ni_2P, with WO_{3-x} nanowires[97]. Even though WO_{3-x} and Ni_2P could by themself catalyse the dehydrogenation, the activity of the catalyst under light irradiation was one order higher than with Ni_2P, and the activity per gram of catalyst was higher than with pure Ni_2P.

Alkali metals or hydrogen can be intercalated to tungsten oxide structure into empty spaces between WO_6 octahedra. Formed channels make possible cation movement. Similar H_2 spillover process approaches to H_xMoO_{3-y} can be used to synthesise tungsten hydrogen bronzes. Pd/H_xWO_3 prepared by this approach has been shown to enhance the catalytic activity of p-nitrophenol reduction[40].

Mo and W belong to the VI group of elements and can be used to form oxides consisting of both of these cations. Yin et al. synthesised $Mo_xW_{1-x}O_{3-y}$ sheets by non-aqueous solvothermal method (Figure 13) that showed a blue-shifted and significantly enhanced LSPR peak compared to monometallic counterparts the group had studied previously[98]. Even though this material showed light-induced catalytical activity for ammonia borane

dehydrogenation, it was even further increased by incorporating Pd-islands on the surface of $MoxW_{1-x}O_{3-y}$[99].

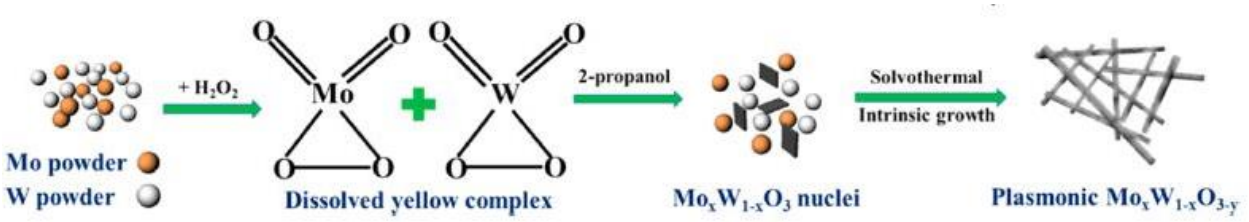

Figure 13. Scheme of synthesis strategy for $Mo_xW_{1-x}O_3$ by Yin et al.[98] *Reprinted with permission from Yin, H.; Kuwahara, Y.; Mori, K.; Cheng, H.; Wen, M.; Huo, Y.; Yamashita, H. Localized Surface Plasmon Resonances in Plasmonic Molybdenum Tungsten Oxide Hybrid for Visible-Light-Enhanced Catalytic Reaction. J. Phys. Chem. C* ***2017****, 121 (42), 23531–23540. Copyright 2017 American Chemical Society*

2.4.6. Copper sulfide

Cation deficient copper sulfide, with a general form of $Cu_{2-x}S$, has several distinct phases dependent on the Cu/S ratio of the material[100]. LSPR in this material arises from the inclusion of free holes caused by the copper deficiency of the material. LSPR lies in the IR region and can be modified by its phase that is tied to free hole density as well as the size and shape of the particles or oxidation and reduction. The crystal structure changes easily with conditions and makes attributing changes to specific parameters complicated.[101,102] According to Xu and colleagues, the most used synthesis strategy is hot-injection[103].

Cui et al. combined the catalytic properties of Pd to plasmonic Cu_7S_4[24]. 14 nm copper sulfide NPs were prepared by solvothermal decomposition from a single precursor, and 4 nm Pd islands were formed with hot injection on the particle surface. Suzuki coupling, nitrobenzene hydrogenation and oxidation of benzyl alcohol reactions were studied, with the highest conversion enhancement under 1500 nm laser irradiation, compared to 808 and 980 nm lasers. (Figure 14). Significant conversion rates were also obtained under simulated solar irradiation and solar light in an outdoor environment. The activity of the hybrid structure significantly exceeded the activity of its constituents, and the fraction of

photothermal effect was deduced low. The prepared structure was extendable to other noble metal /Cu_7S_4 (Pt, Au, Ag) catalysts.

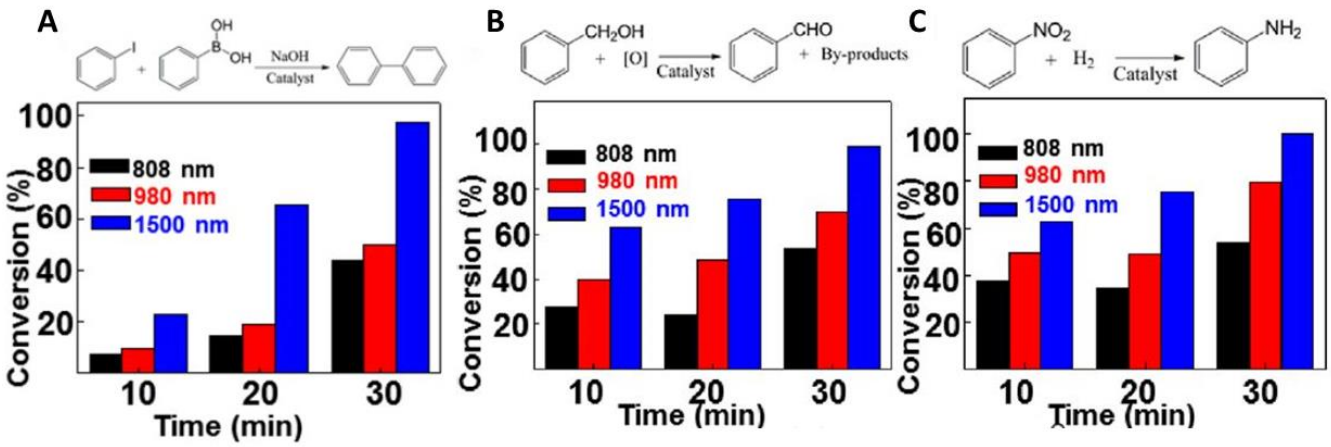

Figure 14. Pd/Cu_7S_4 catalyst efficiency at different wavelengths. A: Suzuki coupling, B: Oxidation of benzyl alcohol C: Nitrobenzene hydrogenation. Reprinted with permission from Cui, J.; Li, Y.; Liu, L.; Chen, L.; Xu, J.; Ma, J.; Fang, G.; Zhu, E.; Wu, H.; Zhao, L.; Wang, L.; Huang, Y. Near-Infrared Plasmonic-Enhanced Solar Energy Harvest for Highly Efficient Photocatalytic Reactions. Nano Lett. ***2015****, 15 (10), 6295–6301. Copyright 2015 American Chemical Society*

Liu and co-workers reported a procedure for preparing $Cu_{2-x}S$ nanowires by cation exchange, with samples of varying composition of x between 0-1[104].(Figure 15) These nanowires were decorated with colloidally prepared Pd NPs, and the system was shown to have enhanced catalytic activity compared to bare copper sulfide nanowires under visible light (λ > 420 nm) in ammonium borane hydrogenation reaction.

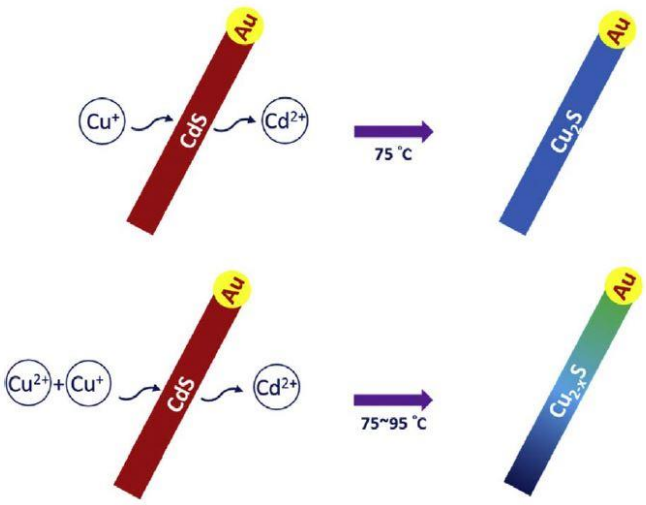

Figure 15. Cation exchange method for preparation of $Cu_{2-x}S$ nanowires. Liu et al.[104] *Reprinted with permission from Liu, P. H.; Wen, M.; Tan, C. S.; Navlani-García, M.; Kuwahara, Y.; Mori, K.; Yamashita, H.; Chen, L. J. Surface Plasmon Resonance Enhancement of Production of H2 from Ammonia Borane Solution with Tunable Cu2−xS Nanowires Decorated by Pd Nanoparticles. Nano Energy* ***2017****, 31, 57–63. Copyright 2017 Elsevier*

2.4.7. Titanium nitride

Titanium nitride (TiN) is a hard, refractory material with metallic behaviour and a high melting point[9]. It has a high carrier density, causing an LSPR absorption at visible or NIR regions[38]. TiN, with other transition metal nitrides, is non-stoichiometric[41]. The preparation method affects the composition, and consequently, the properties of the material. It has been shown that the N/Ti ratio in TiN affects its electrical and optical properties[105,106]. A review by Karaballi et al. lists laser ablation, nitridation of TiO_2 with NH_3 and some other solid-state and plasma methods as suitable for preparing TiN nanoparticles[107]

Titanium nitride has been widely suggested as an alternative to gold because of the similarities in the LSPR absorption, especially in applications where high heat resistance is needed[108,109]. TiN nanoparticles have been used in studies for biomedical applications, for example, photothermal therapy for cancer treatment for its biological compatibility and significant absorption in the biological transparency window in NIR[47,110]. Computational studies have reported TiN to have the most suitable properties for plasmonic applications

among metal nitrides[111]. However, local field enhancement has been described as lower compared to gold[109].

Rej and co-workers formed binary plasmonic catalyst Pt/TiN by decorating TiN cubes with Pt clusters in the presence of formaldehyde in aqueous suspension[112]. In the synthesis, NaOH was used to neutralise the acidity formed in the previous acid treatment of the commercial TiN particles, performed to achieve better attachment of Pt on the TiN surfaces. High-resolution transmission electron microscopy (HRTEM) imaging show Pt clusters well-dispersed on TiN particles. (Figure 16 a, b) Based on energy-dispersive X-ray spectroscopy (EDS, Figure 16, g) and X-ray photoelectron spectroscopy results, the authors reason formation of a self-passivating layer of titanium oxide and titanium oxynitride on the particle surfaces during the catalyst preparation.

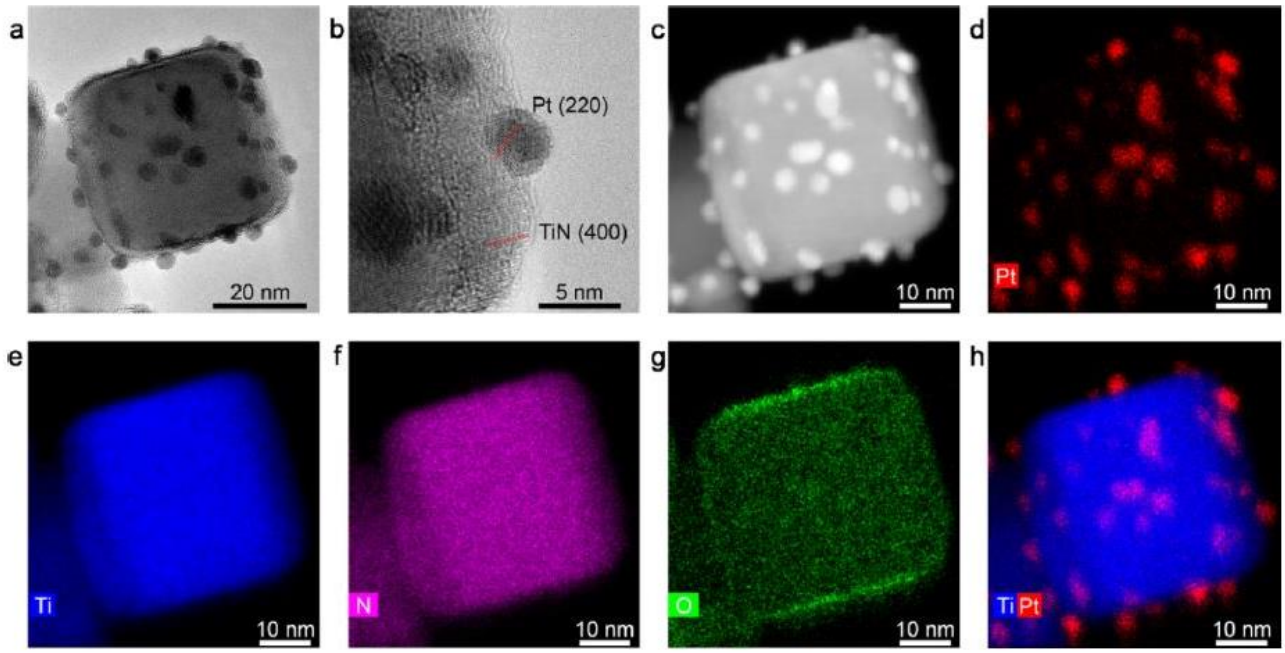

*Figure 16. Pt/TiN catalyst. a: TEM image of a catalytic particle with a TiN cube and Pt islands. b: magnification of a HRTEM image. c: Dark-field scanning TEM image of catalyst hybrid d-h: EDS mapping Pd, Ti, N, O and overlayed Ti and Pd. Reprinted with permission from Rej, S.; Mascaretti, L.; Santiago, E. Y.; Tomanec, O.; Kment, Š.; Wang, Z.; Zbořil, R.; Fornasiero, P.; Govorov, A. O.; Naldoni, A. Determining Plasmonic Hot Electrons and Photothermal Effects during H2 Evolution with TiN-Pt Nanohybrids. ACS Catal. **2020**, 10 (9), 5261–5271. Copyright 2020 American Chemical Society.*

Synthesised catalyst was tested on ammonium borane dehydrogenation reaction. It showed improved catalytic activity under light irradiation, which was contributed to the combined effects of photothermal heating and hot carrier formation in TiN and Pt particles. Hot electrons were constituted to decrease the activation energy required to reach the transition state of the downhill reaction of H_2 formation.

Li and co-workers formed nanocomposite TiO_2 /TiN photocatalyst by hydrothermal vapour phase growth of TiO_2 particles on TiN[53]. With this system, good visible-light enhanced catalytic activity was observed for the degradation of organic pollutants Rhodamine B and 4-nitrophenol and disinfection of micro-organisms of *E. coli.* The proposed method of catalysis is driven via hot electron induced $\bullet O_2^-$ and consecutive formation of •OH-, depicted in Figure 17.

Cr-doped titania was used by Kaur et al., who also studied plasmonic TiN based materials for environmental degradation applications[113]. TiN in SiO_2 shell decorated with Cr-doped TiO_2 was successfully used for the photodecomposition of methylene blue. Formed nanoparticles were supported in gel-like transparent calcium alginate beads to obtain a floating catalyst with easier reusability.

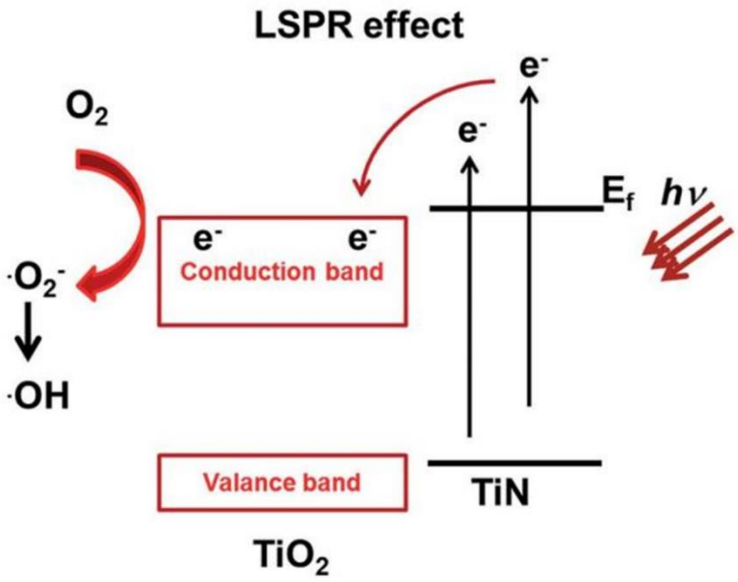

Figure 17. Proposed photocatalytic mechanism of TiO_2/TiN nanocomposite catalyst. Reproduced with permission from Li, C.; Yang, W.; Liu, L.; Sun, W.; Li, Q. In Situ Growth of TiO2 on TiN Nanoparticles for Non-Noble-Metal Plasmonic Photocatalysis. RSC Adv. ***2016****, 6 (76), 72659–72669. Copyright 2016 The Royal Society of Chemistry*

2.4.8. Tantalum Carbide

Tantalum carbide has been described as a conductive, hard material with strong and broad resonance[114]. In a computational study, Kumar et al. utilised first-principle DFT to investigate conductive ceramics proposed as promising materials for non-metal plasmonics[111]. According to their dielectric functions, metal carbides were described as unsuitable for plasmonic applications due to their high losses in the visible and NIR region. However, upon examining the scattering and absorption efficiencies, TaC was suggested, together with TiN, to have the best properties for photothermal applications from the included carbides and nitrides.

This feature has been employed in some hybrid catalyst applications. Anjaneyulu and co-workers prepared Co/TaC catalyst by precursor reduction in an organic solvent and subsequent annealing[115] (Figure 18). The absorption maximum of the catalyst was measured to approximately 500 nm. In DRM reaction under light irradiation, Co/TaC particles showed higher activity than Co-clusters supported on alumina.

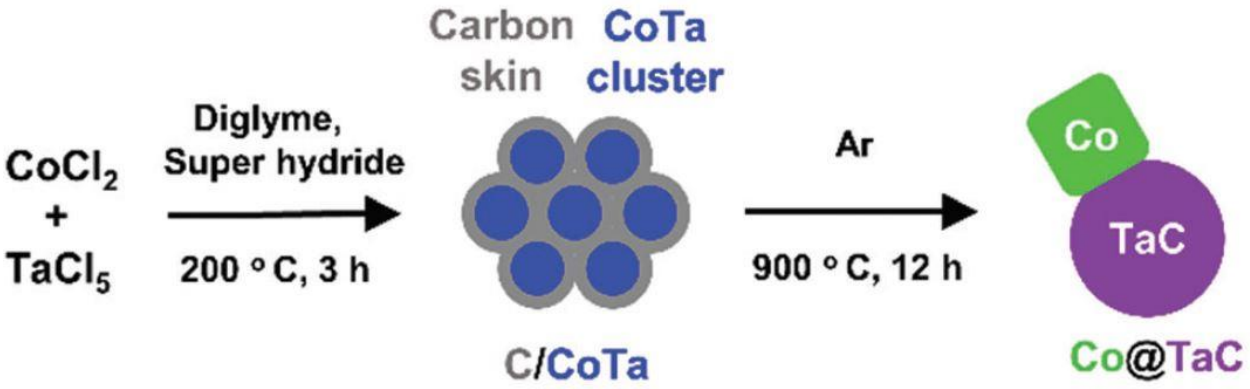

Figure 18. Schematics of a Co/TaC (Co@TaC) catalyst synthesis. Reprinted with permission from Anjaneyulu, O.; Takeda, K.; Ishii, S.; Ueda, S.; Nagao, T.; Xiaobo, P.; Fujita, T.; Miyauchi, M.; Abe, H. Light-Promoted Conversion of Greenhouse Gases over Plasmonic Metal-Carbide Nanocomposite Catalysts. Mater. Chem. Front. ***2018****, 2 (3), 580–584. Copyright 2018 The Royal Society of Chemistry*

Later by the same group, Ni/TaC hybrids were composed by impregnating commercial TaC particles with Ni[114]. Again, the catalyst was used for DRM reactions. The authors report TaC to enhance reaction activity via effects of photothermal heating and lowered coking rate.

2.5. Final remarks from the literature review

This section presented hybrid catalysts with sustainable, earth-abundant plasmonic materials. In a short time, many studies have approached the question of a hybrid plasmonic catalyst with different materials, methods and studied reactions. Whereas some work focused mainly to prove the concept, other, more recent work has targeted industrially and environmentally essential reactions.

Even though examining earth-abundant plasmonic materials has been a motivation in these studies, few have paid attention to the sustainable considerations of the catalytical part of the system. Perhaps in the future, with development and deeper understanding of the plasmonic part, earth-abundant alternatives will be studied also in these materials. Practical use and synthesis of many described materials is hindered by oxidation in the

air and less-developed synthesis methods. More work needs to be done to overcome these challenges and make these catalysts practical for large-scale applications.

3. Experimental work

3.1. Aim of the study

The work aimed to study an earth-abundant alternative plasmonic material for photocatalysis. This objective was approached by synthesising and studying catalytical reactions of a hybrid Pd/TiN catalyst and differences in catalytic activity under light irradiation and in dark. Palladium was chosen as a catalytic material for its well-established catalytical chemistry and activity in various chemical reactions[116]. The focus of this work was on studying the performance of TiN as the plasmonic component in the system. In the following work on this topic, exchanging Pd for a more earth-abundant alternative or minimising its use could be studied.

3.2. Methods

3.2.1. Materials and methods

Titanium nitride (50 nm and 20 nm) were purchased from PlasmaChem. Titanium nitride (<3 μm), Potassium tetrachloropalladate(II), (K_2PdCl_4, 98%), L-lysine (≥98%) polyvinylpyrrolidone (PVP, MW. 55 000 g/mol), sodium borohydride (Fine granular for synthesis), phenylacetylene (98%) ammonia-borane complex (97 %) and nitric acid (65 %, for synthesis) were purchased from Sigma-Aldrich. Ethanol (p.a.) and 2-propanol (IPA) were used from Honeywell. Hydrochloric acid (37 %) was purchased from VWR. All materials were used without further purification. Deionised water was used throughout all experiments.

3.2.2. Synthesis of Pd/TiN NPs

3.2.2.1. Reduction with $NaBH_4$

Palladium clusters were reduced on the commercial TiN particles using sodium borohydride ($NaBH_4$) and L-lysine in water suspension. Two different sizes of TiN particles, <3 µm and 50 nm, were used, and the Pd loading was changed between samples. The sizes mentioned are particle sizes given by the manufacturers. Table 1 presents prepared catalysts and materials used for them.

In the reduction procedure (Figure 19), 500 mg of TiN was placed in a beaker, and Pd-precursor and L-lysine solutions were added. The suspension was stirred covered at room temperature for 30 min. Just before addition, $NaBH_4$ was dissolved in water and then added dropwise to the stirring suspension. The suspension was stirred once more for 30 min. The suspension was let to settle overnight. It was centrifuged and washed three times with water and once with ethanol. The catalyst was dried overnight in air at 60 °C. The catalyst was ground with mortar before storage and use.

Table 1. Prepared catalysts and materials used in their synthesis.

Size (TiN)	Pd loading (wt-%)	Pd-precursor (0.01 M, mL)	Lysine (0.53 M, mL)	$NaBH_4$ (g)
<3µm	3	14.1	10	0.013
	0.5	2.349	10	0.013
	0.05	0.235	5	0.0065
	0.01	0.0469	5	0.0065
50 nm	3	14.1	10	0.013
	0.05	2.14 (0.0011 M)	10	0.008

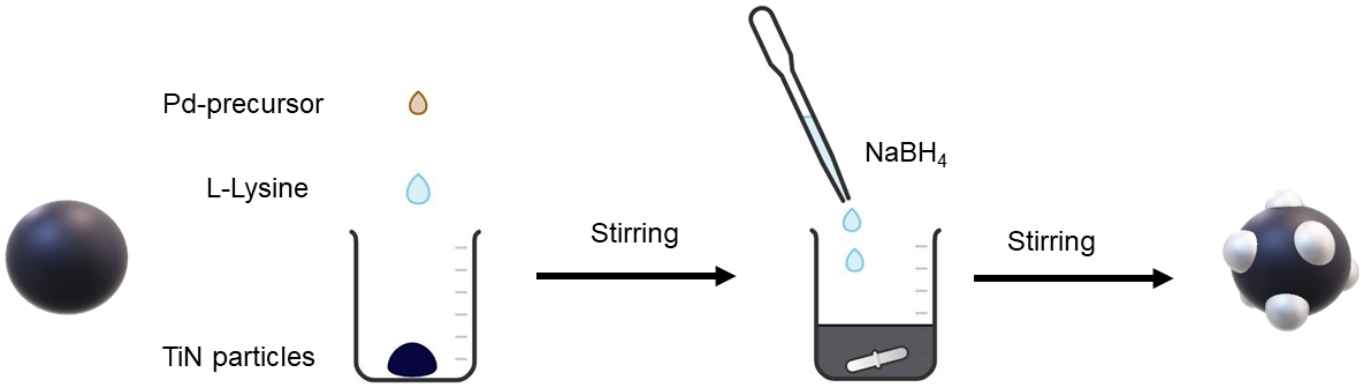

Figure 19. Scheme of the $NaBH_4$ assisted synthesis

3.2.2.2. Reduction with ethanol and polyvinylpyrrolidone

This approach was adapted from the work of Cardoso et al.[117] In their work, Pd islands were reduced on carbon nanotubes. This synthesis method was tried to see any possible difference in resulting catalysts characteristics and performance compared to the catalyst prepared by the $NaBH_4$ reduction method. In the modified procedure, PVP was dissolved in 12 mL of ethanol TiN (112 mg, <3 µm). Ethanol (6 mL) and prepared solution were added to two neck round-bottom-flask and stirred for 15 min in an oil bath (75 °C). The Pd precursor was added (0.005 M in water, 1 mL) dropwise and stirred for 3 h. Let to cool down and settle overnight. The catalyst was washed five times with ethanol and dried in air overnight (60 °C).

3.2.3. Characterisation

3.2.3.1. UV-Vis spectrophotometry and diffuse reflectance spectroscopy

Spectrophotometry is a relatively simple and widely used method for sample characterisation. In the measurement, transmission or reflection of light is measured as a function of measurement wavelength. Description UV – Vis is usually used to define the

used wavelength to the ultraviolet and visible light range. In the simplest transmission measurement, light power attenuation in the measurement sample is gauged. Typically, measured transmission or reflectance results are recalculated and reported as absorption, assuming that the sample absorption causes all light power loss in the measurement.[118]

Light absorption in the sample can cause atomic or electronic movement; therefore, measuring spectrophotometric spectra can be beneficial to the characterisation of the electronic and atomic structure of the sample. If the plasmon excitation of the material lies in the measurement wavelength range, it can also be characterised. Many different factors can affect the spectra, for example, temperature, stress, morphology or the surrounding medium. These factors should be held constant to give comparable results.

Diffuse reflectance is a method of spectrophotometry for solid, opaque samples with a rough sample surface. Commonly measured samples are, among others, powders, ceramics and nanostructures. Measured is the reflectance of the sample surface to all directions, compared to a reference with high reflectance using special mirrors or an integrating sphere.[118] (Figure 20)

UV-Vis Spectrometry (UV-Vis) measurements were performed with Shimadzu UV-2600 in the range of 200-800 nm. Sample suspensions were prepared by dispersing a small, arbitrary amount of solid sample in water. If needed, the suspension was diluted and measured again to give an absorption maximum smaller than 1.

Diffuse reflectance spectroscopy measurements were performed with the same instrument with an integrating sphere attachment. Samples were prepared either by pressing the sample into the sample holder or with drop-casting acetone slurry. Barium sulfate was used as a reference.

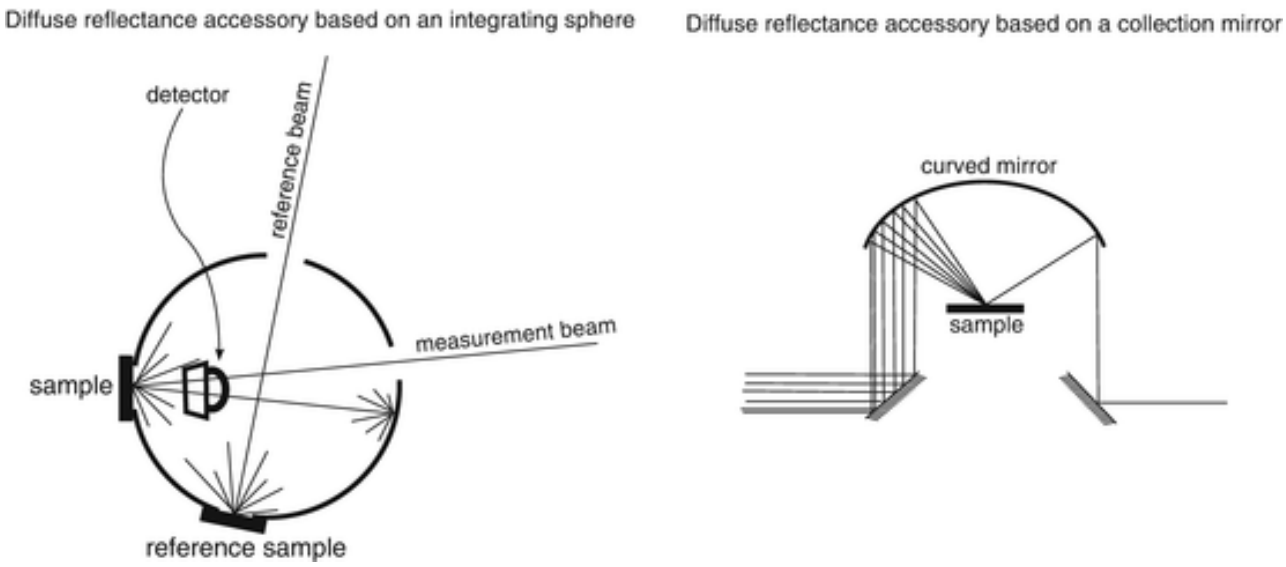

Figure 20. Integrating sphere attachment (left) and a collection mirror (right) for DRS. Reprinted with permission from Soares, J. A. N. T. Introduction to Optical Characterization of Materials. In Practical Materials Characterization; Sardela, M., Ed.; Springer New York: 2014; pp 43–92 Copyright 2014 Springer Nature

3.2.3.2. Scanning electron microscopy

Scanning electron microscopy (SEM) is a widely used electron microscopy for imaging materials and their surfaces. In this method, high magnification images of the specimens are obtained by scanning the surface point-by-point with a focused electron beam. The depth of field of the image causes the image to appear three-dimensional, similar to what could be “seen” with the eye if it would be capable of such magnification. A flow of electrons is formed in an electron gun and focused with a set of electron lenses. With the last lens, the electrons are focused on the point of interest in the specimen (Figure 21). When electrons hit the surface, electrons interact with the material and are emitted back outside the specimen. These signal electrons are backscattered and secondary electrons, either scattered from the material surface or ejected from the specimen atoms. Part of these signal electrons are detected, amplified and translated to form one part of the image. Each of these measured signals constitutes one point in the final image. The SEM can cover a large scale of magnification with image resolution governed by electron beam brightness and diameter of the electron beam at the specimen.[119,120]

In this work, samples of commercial TiN and 3 % Pd/TiN of both particle sizes were imaged. (Hitachi S-4800 Field Emission Scanning Electron Microscope). All SEM samples were prepared by drop-casting. A small drop of sample suspension (in H_20) was dropped on a Si substrate attached to a sample holder by carbon tape and let dry overnight.

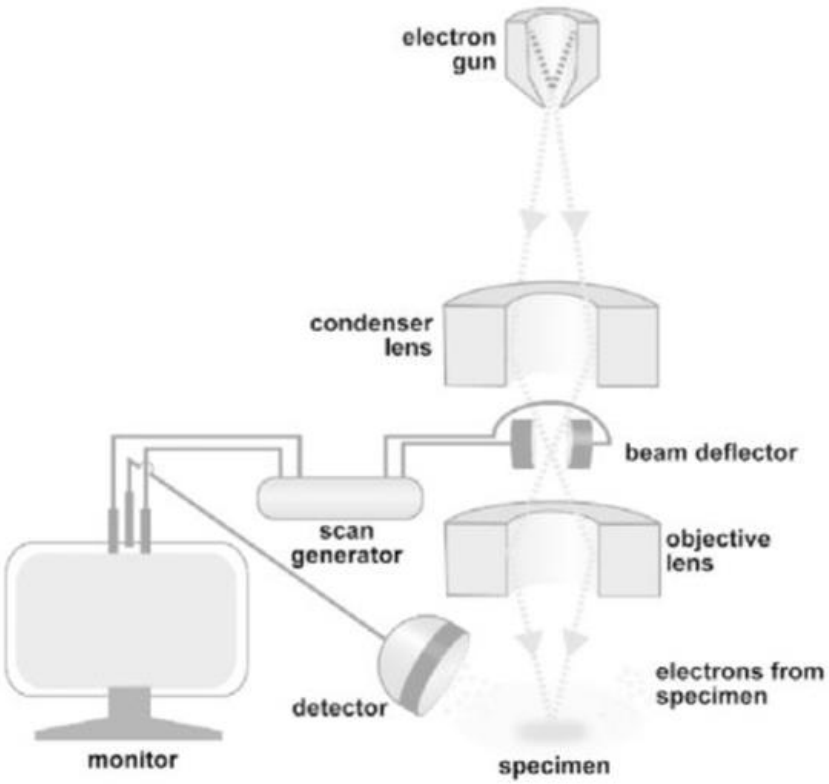

Figure 21. Schematic image of a SEM device. Reproduced from Schatten, H. The Role of Scanning Electron Microscopy in Cell and Molecular Biology: SEM Basics, Past Accomplishments, and New Frontiers. In Scanning Electron Microscopy for the Life Sciences; Cambridge University Press, 2012; pp 1–15 with permission of Cambridge University Press through PLSclear. Copyright 2012 Cambridge University Press.

3.2.3.3. Microwave plasma atomic emission spectrometry

Atomic emission spectrometry is a method of analysing elemental concentrations of measured samples by measuring their light emission intensities from excited states. Microwave refers to how the plasma is formed in the microwave plasma atomic emission s (MP AES) instrument. In the analysis, the sample is lead to a high-temperature plasma cell, where the liquid sample is transformed to free atoms and ions. The high temperature of the surroundings excites particles to their unstable excited electronic states. Return to the ground states causes light emissions of wavelengths typical to each ion or atom. Analysing the spectra and intensities of the radiation can be used to determine the concentrations of elements of interest.[121]

The instrument for atomic emission spectrometry can be divided to signal generator and signal processor units. The former part consists of sample introduction and plasma source, the latter of optics, electronics and data acquisition.[121] Schematic picture of the measurement is presented in Figure 22. In addition to plasma sources, flame and electronic spark ark can be utilised to form excited atoms and ions. However, plasma sources are preferred due to their higher temperature that corresponds to higher emission intensity.[122]

Calibration of the measurement is performed using a calibration series. Sample concentration can be determined using calibration curves of standards of known concentrations and their measured intensities. To precise measurement, emissions at different wavelengths are used to calculate the sample concentration. The palladium content of two catalysts was analysed with a microwave plasma atomic emission spectrometer. (Agilent technologies 4200 MP AES).

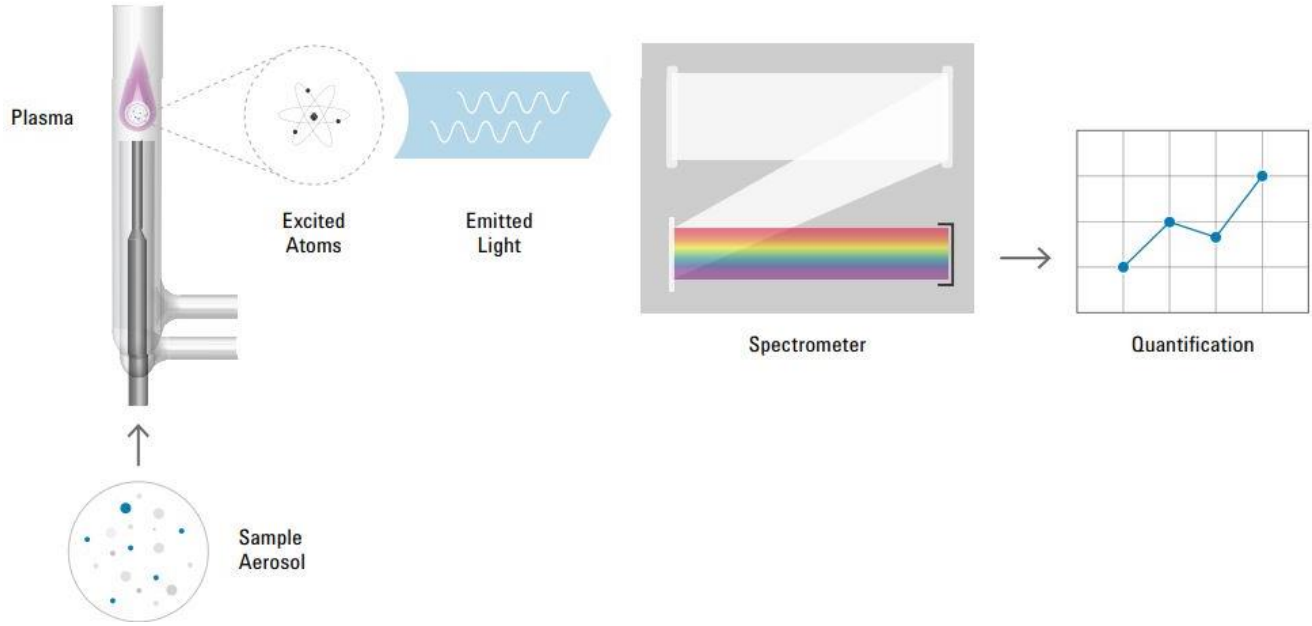

Figure 22. Schematic diagram of MP AES instrument. Reproduced with permission from Microwave Plasma Atomic Emission Spectroscopy (MP-AES) Application eHandbook, January 2021 Edition https://www.agilent.com/cs/library/applications/5991-7282EN_MP-AES-eBook.pdf, accessed 9.2.2021. Agilent.

A sample of 3 % Pd/TiN (<3µm) was prepared by boiling a known mass of catalyst (12.4 mg) in 5 mL of aqua regia in a round-bottom flask with a condenser. In the process, the catalyst was dissolved. The sample was centrifuged, but no solid was observed in the solution. Then, the solution was transferred to a clean round-bottom flask, and the centrifuge tube was washed with approximately 5 mL of water and centrifuged. The centrifuged solution was added to the previously transferred solution, and excess solvent was evaporated by boiling the solution. The remaining solution was diluted with 0.5 M HCl in a volumetric flask (100 mL). This approach for sample digestion was adopted from the previous sample preparation made in the group. However, as no solid was formed during the procedure, it could be simplified.

For 3 % Pd/TiN (50nm), two replicate samples (6.95 mg, 10.05 mg) were prepared by boiling samples under reflux in aqua regia (5 mL, 15 min). After cooling, the solutions were centrifuged to remove possible solids. No solids were observed. The solution was transferred to volumetric flasks (100 mL) and filled with 0.5 M HCl.

Sample concentration was determined with a calibration series. The series was prepared by diluting a primary solution (61.0 ppm) to suitable concentrations in volumetric flasks (10 mL). All dilutions were done using 0.5 M HCl. Table 2 contains concentrations of the standards and volumes of primary solutions used.

Table 2. Standard series for MP AES measurement.

	c (ppm)	Addition (µL)
blank	0	0
std1	0.1	16.4
std2	0.3	49.2
std3	1.1	180
std4	2.2	360
std5	5.5	901

3.2.3.4. X-ray diffraction

X-ray diffraction (XRD) is used to determine properties of polycrystalline materials by probing the samples with an X-ray beam. As a result of a scan over a range of incident angles, information on the interatomic spacing of the material is obtained and can be used to identify the phases present.

X-rays scattered from crystal planes form constructive interference patterns that can be observed as diffraction peaks. These patterns are governed by Bragg's law:

$$2d\ sin\ \theta\ =\ \lambda \qquad (5)$$

Braggs' law connects the diffraction angle (θ) and the wavelength (λ) of the source radiation to interplanar spacing (d). A measurement over a suitable angular range gives a pattern of diffraction peaks, from which information of the material can be resolved. Commonly, diffraction data is used to phase identification. Diffraction peak positions can be compared with a database of reference patterns to determine the chemical composition and crystalline structure of the measured material. With further data treatment, information about the relative amounts of the phases present, crystallinity and

structural properties can be obtained.[123,124] A schematic drawing of an XRD measurement is depicted in Figure 23.

A powder diffraction scan of 3 % Pd/TiN (<3 µm) and 3 % Pd/TiN (50 nm) were performed (X'Pert PRO PANalytical). Samples were prepared by front-loading the catalyst into the sample holder. The measurements were done with Cu K_α radiation in the range of 10-90° with a step size of 0.052° and a step time of 1.2 s. Measurement data was analysed with HighScore software.

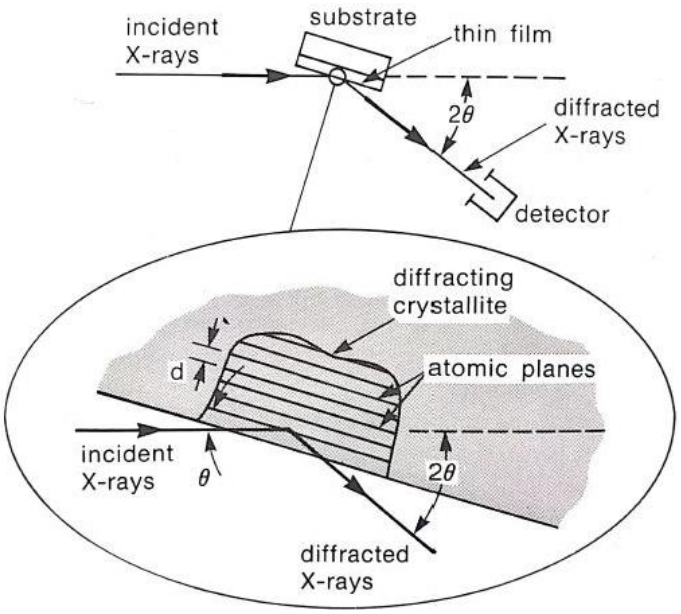

Figure 23. Schematic image of an XRD measurement. Reprinted from Toney, M. XRD X-Ray Diffraction. In Encyclopedia of materials characterization : surfaces, interfaces, thin films; Brundle, C. R., Evans, C. A., Fitzpatrick, L. E., Wilson, S., Eds. Copyright 1992, with permission from Elsevier

3.2.4. Catalytic studies

Catalytic reactions were performed to study the effect of light irradiation on catalyst performance.

3.2.4.1. Phenylacetylene hydrogenation

Phenylacetylene reacts in the presence of H_2 to form two main reaction products, ethylbenzene and styrene (Figure 24). The reaction is used as a model reaction for selective alkyne hydrogenation in mild reaction conditions. With two different main products, in addition to the total conversion, steering the selectivity of the reaction is also a property of interest. Removal of unwanted phenylacetylene and high formation of styrene is in the interest of the chemical industry in the styrene fabrication processes.[125]

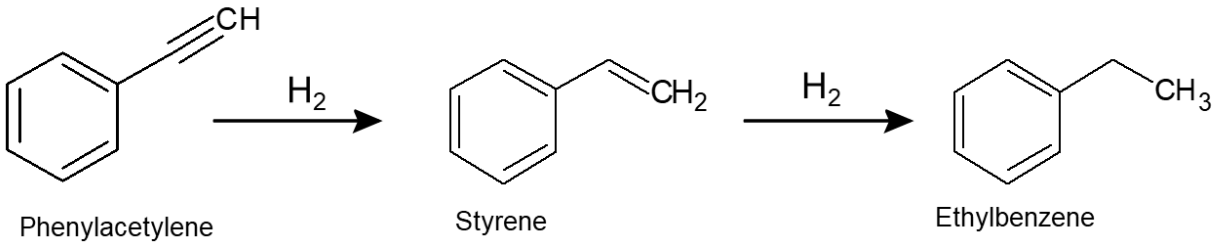

Figure 24. Phenylacetylene hydrogenation reaction.

In the reaction procedure, a catalyst was added to a round-bottom flask. A solution of 0.1 M phenylacetylene in IPA (3 mL) was added. The reaction flask was connected to a glass adapter with a connected H_2 filled balloon. The connection was sealed with parafilm. Reactions performed in dark were wrapped in aluminium foil, and heated reactions were immersed in a pre-heated oil bath with controlled temperature. Light reactions were done in a light-box attached with a LED lamp (450 nm) (Figure 25). After the reaction time, samples from the suspension were taken by syringe and filtered with filter to a gas chromatography (GC) vial.

Figure 25. Used light-box with an attached light on a stirring plate.

The concentrations of reagents and products were measured by gas chromatography (Shimadzu Nexis GC-2030). Peak areas for phenylacetylene, ethylbenzene, styrene and homocoupling products were used. In the first part of the reactions, the reaction was optimised to show a small conversion in the dark. The parameters varied in this step were reaction temperature and time, the catalyst used (metal loading), catalyst mass, and phenylacetylene concentration.

In the second part were done reactions with comparable light and dark conditions. It was observed that the reaction was heated due to light irradiation. The effect of light heating was studied on the solvent. A glass vial containing IPA (3 mL) was set to the light-box. A thermometer was placed in the solution and sealed with parafilm. The temperature of the solvent was observed at set intervals. Catalysts with <3 μm TiN particles were used for all phenylacetylene hydrogenation reactions. Phenylacetylene hydrogenation was not studied with Pd/TiN catalyst with 50 nm TiN, because the small size of the particles made

it difficult to separate them from the liquid phase reliably enough to perform gas chromatography.

3.2.4.2. Ammonium borane dehydrogenation

Ammonium borane reacts with water in the following reaction:

$$NH_3BH_3 + H_2O \rightarrow NH_4^+B(OH)_4^- + 3H_2\ (g)$$

Where 1 mol of ammonium borane produces 3 mol of hydrogen[112]. It was chosen as a studied reaction with a simple approach to see plasmonic enhancement effect on the reaction before proceeding to other, possibly more complicated reactions.

The reaction was followed by capturing the gas formed in the reaction and leading it with a tube to an upturned volumetric cylinder immersed in water. The amount of gas in the cylinder was followed by the water level in the cylinder. The reaction set-up is depicted in Figure 26.

After some optimisation, the following procedure was used: 3 % Pd/TiN (50 nm) catalyst (5.7 mg) was dispersed in reaction flask with 4 mL of H_2O and sonicated (5 min). Ammonium borane (10 mg) was dissolved in 1 mL of H_2O by shaking in a 2 mL Eppendorf tube right before it was added to the reaction flask. The flask was attached to a tube and sealed with parafilm. The water level in the volumetric cylinder was followed through the reaction.

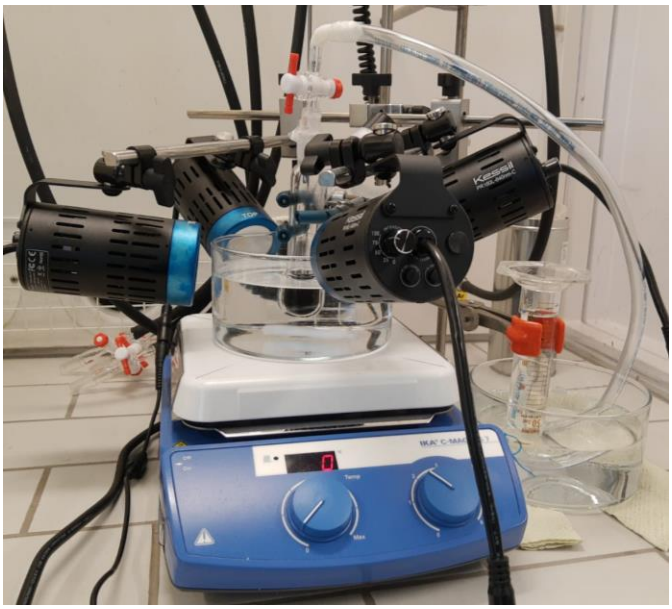

Figure 26. Set-up for ammonium borane dehydrogenation reaction

3.2.5. Supporting

TiN particles were attempted to support on silica to see if the supporting of catalyst would be possible with these methods. Supported catalyst is easier to handle in the washing steps and make easier the GC sample preparation for catalysts with smaller particle size. Two different approaches were used.

3.2.5.1. Dry impregnation

This method was used following a study of Quiroz et al.[126] TiN (50nm, 3 mg) was dispersed in 5 mL of ethanol. Silica (100 mg) was placed in a petri dish. At a time, approx. 0.5 mL of the suspension was added on the silica, and the slurry was mixed with a spatula. The mix was dried in oven (80 °C, 10 min). This procedure was repeated until all the TiN suspension was consumed. Let to dry in the oven overnight.

3.2.5.2. Wet impregnation

The approach was adopted from the work of Rodrigues et al.[127] TiN (50 nm, 3 mg) was dispersed in water (3.5 mL). The formed suspension and silica (100 mg) were stirred in a covered beaker at room temperature for 23 h. After stopping the stirring, white particles in a dark liquid were observed. It was deduced that dark TiN particles did not attach to white silica particles.

The procedure was repeated, exchanging H_2O for ethanol. After the stirring, the suspension seemed uniform, but after centrifuging, white particles settled in dark liquid. The same was observed with the sample from dry impregnation. It was concluded that these methods with tried parameters were not suitable for supporting TiN particles, and therefore not suitable for supporting the studied Pd/TiN particles.

3.3. Results

3.3.1. Characterisation

DRS spectra for <3 µm and 50 nm TiN and 3 % Pd/TiN <3 µm are shown in Figure 27. The spectra are normalised at 250 nm. The figure shows a maximum absorption presumed to be related to the LSPR excitation at 450 nm for <3 µm TiN particles. The absorption maximum for smaller particles is shifted to higher wavelengths. The spectra with different sized TiN particles have different shapes, with 50 nm sized particle spectra absorption on the right of the maximum not decreasing as rapidly as for TiN <3 µm samples. Pd containing catalyst has a slightly damped absorption compared to the pure TiN particles. According to these results, blue light (450 nm) was used in phenylacetylene hydrogenation reactions.

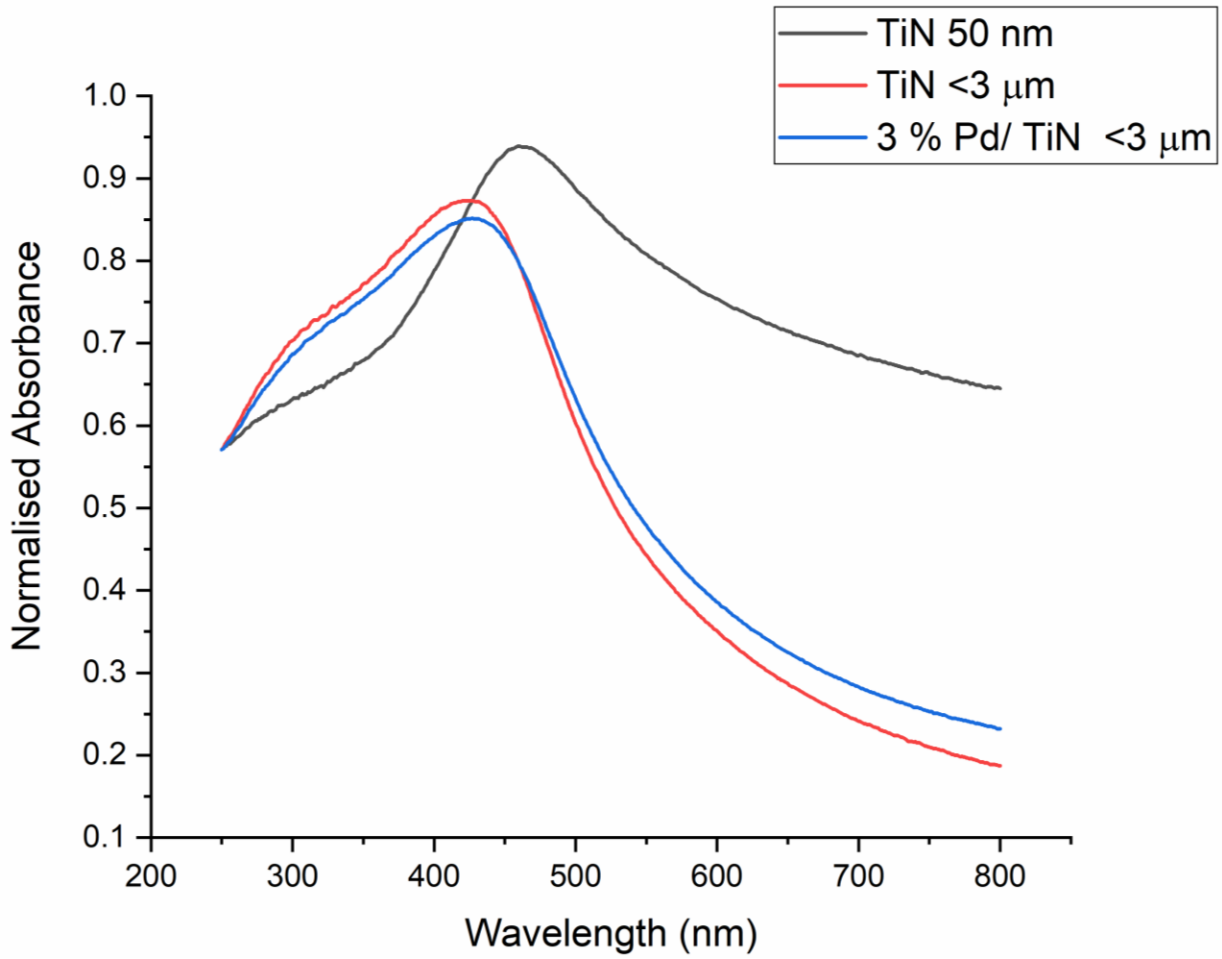

Figure 27. DRS spectra of TiN <3 µm, 3% Pd/TiN <3 µm and TiN 50 nm

The measured UV-Vis spectra of samples suspended in water are shown in Figure 28. The measurement range was 200-800 nm. The data was normalised to values 0-1 for each measurement and then set the lowest point in the area of 450 nm to 0 absorbance. Between 20 nm, 50 nm and <3 µm particles, 50 nm TiN particles have the highest absorption, with maximum absorption at approximately 680 nm, while 20 nm and <3 µm particles have lower absorption and the maximum in the absorption is red-shifted. These suspension measurements were used to decide to use red light (640 nm) for ammonium borane dehydrogenation reactions. For TiN with different Pd-loadings (all 50 nm TiN Figure 28, right), the absorption is slightly damped with increasing Pd-loading.

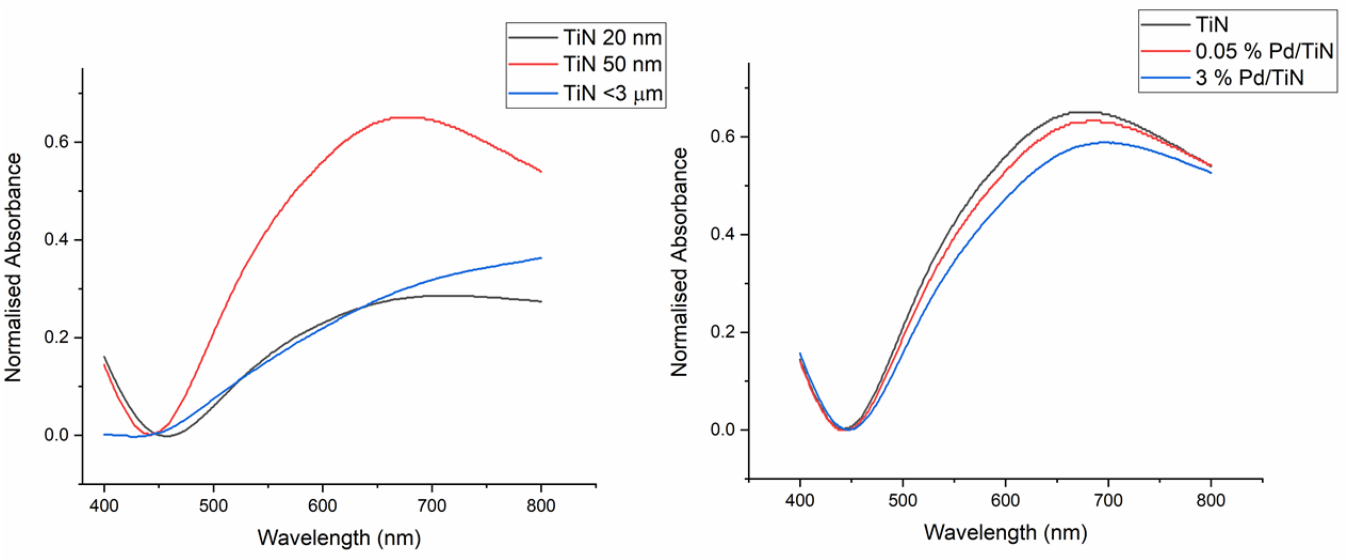

Figure 28. Normalised UV-Vis spectra of particle suspensions. Left: commercial TiN particles of different sizes. Right: 50 nm TiN and Pd/TiN catalysts with varying Pd loading.

Figure 29 presents SEM images of commercial TiN (<3 µm and 50 nm) and synthesised 3 % Pd/TiN catalysts (<3 µm and 50 nm). <3 µm TiN particles are larger particles with uneven surfaces. The surfaces are less rough in the catalyst image. In catalyst, small islands are dispersed on the surfaces; however, they are in small areas close to each other. 50 nm TiN consists of small particles. The size distribution is smaller in the commercial particles than in the catalyst. In the 3 % Pd/ TiN 50 nm image, Pd visible in the lower-right corner is aggregated to one larger cluster. This data indicates that the Pd deposition and uniform distribution over the support requires further optimisations.

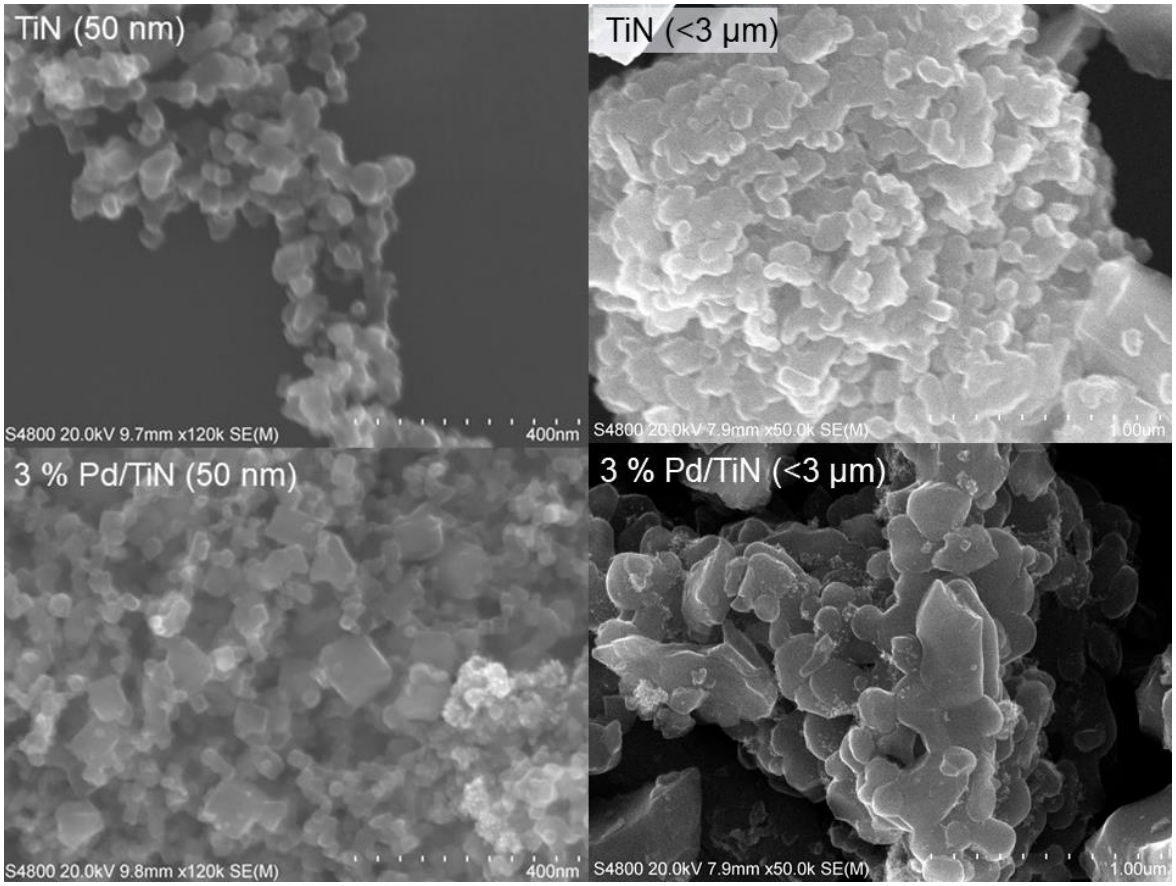

Figure 29. SEM images of commercial TiN and synthesised 3 % Pd/TiN catalysts (<3 μm and 50 nm sizes)

Diffractograms for the catalyst samples are presented in Figure 30. ICDD (International Centre for Diffraction Data) database was used as a reference. The peaks observed in the data were identified as peaks for cubic TiN and cubic Pd. In both diffractograms, peaks for TiN are narrow, resembling to high crystallinity of the nitride. Peaks for palladium are smaller, corresponding to the much smaller amount of metal in the sample. Small peaks prevented analysing the palladium. Especially for the most prominent Pd peaks at 40°, tails from the adjacent TiN peaks overlap with the Pd peak and complicate discerning the peak.

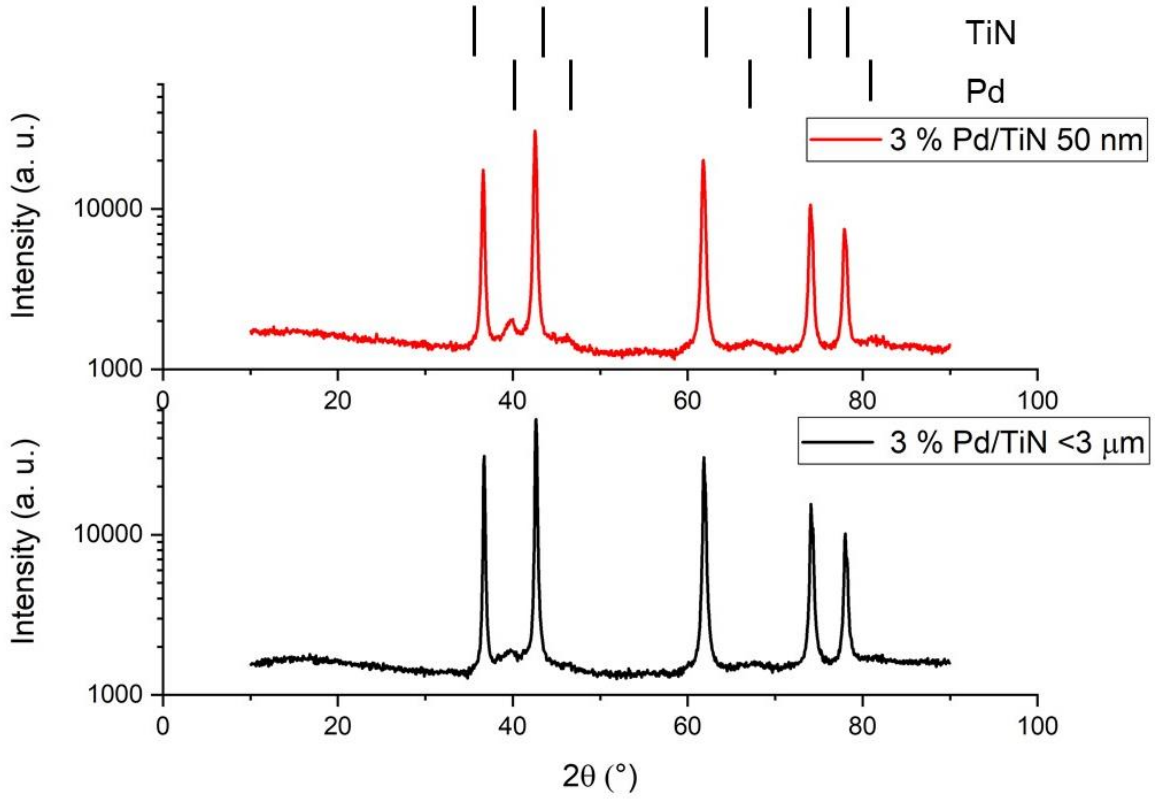

Figure 30. Diffractograms for 3 % Pd/TiN (<3 μm) (black) and 3 % Pd/TiN (50 nm) (red).

In MP AES measurements, calibration curves were used to calculate the sample concentrations. The procedure for obtaining this with 3% Pd/TiN (50 nm) is presented here. For 3 % Pd/TiN (<3μm), a similar treatment was performed in the measurement software of the instrument. First, calibration points at each measured emission wavelength of concentration against emitted intensity were plotted in graphing software (OriginPro 2018b). The plotted points were fitted with a linear fit with a least-square method and intercept at 0. The slope of the fit could be used to interpolate at the sample emission intensity:

$$consentration = A * intensity \quad (6)$$

A is the slope of the fit.

Next, Pd concentrations at all four measurement wavelengths for both samples were calculated with obtained slope values and equation (6). The obtained slopes and graphs

of the fitting can be found in Appendix (Figure A and Table A). The average of the values at different wavelengths was considered as the concentration for the single replicate sample. These values are 2.08 and 2.95 ppm for sample 1 and 2, respectively. Further, these values were converted to the weight-% of the catalyst sample and averaged. According to the performed measurements and data treatment, the Pd-loading of 3% Pd/TiN (50 nm) was 3.0 %. For the other analysed catalyst (3% Pd/TiN (<3 μm)) the measurement and data treated in the measurement software showed a concentration of 3.69 ppm, which corresponds to 3.0 % Pd-loading of the catalyst.

3.3.2. Catalytic studies

3.3.2.1. Phenylacetylene hydrogenation

GC peak areas were recalculated to conversion and selectivity percentages using a calibration series[128] (Figure 31). Calibration points were fitted in Microsoft Excel were to give the following equation:

$$c = A * pa \quad (7)$$

Where *c* is concentration, *A* slope of the fitted line and *pa* peak area obtained from the GC measurement.

Phenylacetylene conversion was calculated:

$$conversion\ (\%) = \frac{c(PA_i) - c(PA_f)}{c(PA_i)} * 100 \quad (8)$$

Where $c(PA_i)$ and $c(PA_f)$ are initial and final phenylacetylene concentrations. For selectivity calculations:

$$selectivity\ (\%) = \frac{c(styrene)}{c(PA_i) - c(PA_f)} * 100 \quad (9)$$

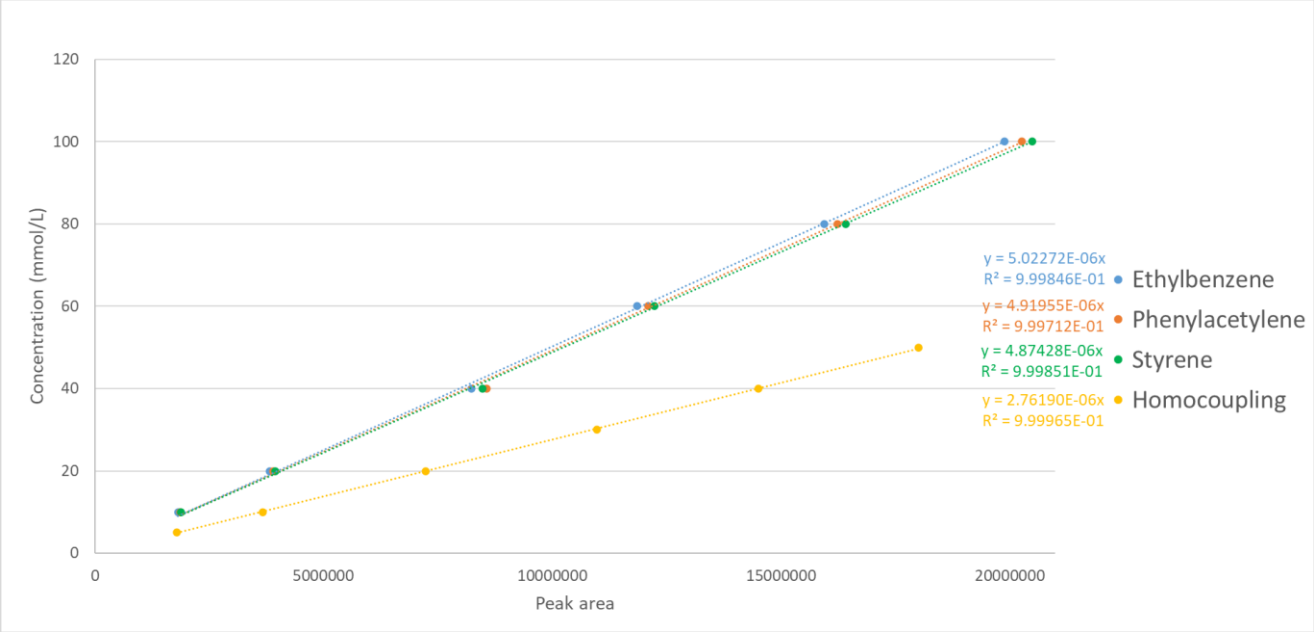

Figure 31. Calibration curves for analysing GC results of phenylacetylene hydrogenation reactions.

Where $c(styrene)$ is the styrene concentration at the end. Similarly, selectivities for ethylbenzene and homocoupling products were calculated. Throughout all reactions, the amount of measured homocoupling products was negligible. In some reactions, selectivity values for styrene or ethylbenzene exceeded 100 %. Therefore, the sum of selectivities was normalised to 100 %, and given values are percentages of this sum.

The optimisation reactions for dark are shown in Appendix (Table B). Suitable, 7 % conversion was reached with 1 h reaction time and 0.05 % Pd/TiN catalyst. Figure 32 shows results for 1 hour and 3-hour reactions in both light and dark. The dark reactions were performed at 40 °C to consider the heating caused by the lamp, chosen according to the solvent heating measurements.

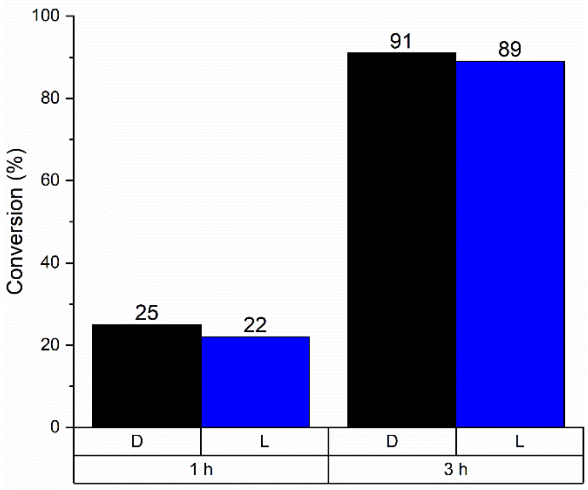

Figure 32. Comparison of phenylacetylene hydrogenation reactions in the dark and under light irradiation.

Opposite to the expected, the conversion of the dark reactions was higher than in reactions performed in light. The selectivity of the reaction did not show any difference between light and dark. (Figure 33, A). The repeatability of the light reaction was studied by repeating the 1 h light reaction. A wide variation in results is apparent; conversion for the reaction was between 19 – 54 %. (Figure 33, B). This can originate from poor control of the light-box temperature during the light measurement and complicated handling during the setting of the light-box reactions. The temperature was shown to affect the reactions; however, the results suggest poor repeatability of the system, which cannot be explained by the same considerations as in light experiments because neither light nor light-box was used. (Figure 33, C). A complete table of the studied reactions can be found in Appendix (Table C).

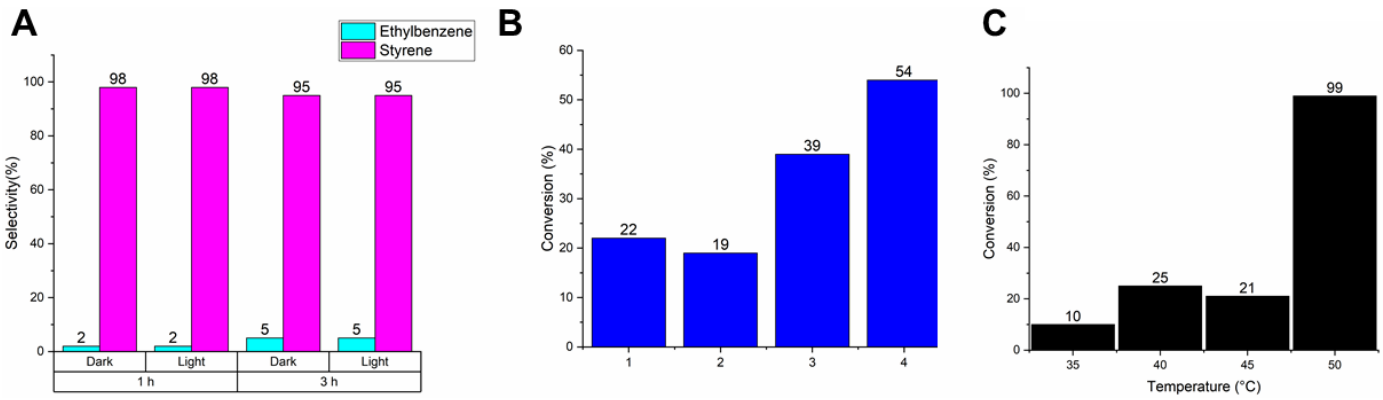

Figure 33. A: Selectivity of performed phenylacetylene hydrogenation reactions. B: Repeatability of reaction under light irradiation. C: Conversion in dark reactions as a function of the reaction temperature.

Phenylacetylene hydrogenation with 0.5 % Pd/TiN reduced with EtOH and PVP was studied. However, the conversion in these reactions was significantly lower than in the comparable reactions done with $NaBH_4$ reduced catalyst, and the reproducibility of the reactions was low. $NaBH_4$ reduction method was chosen for further studies as the better alternative of these two reduction methods.

3.3.2.2. Ammonium borane dehydrogenation

Ammonium borane dehydrogenation reactions in dark and light are presented in Figure 34 (A). However, the four lamps used significantly increased the temperature of the oil bath in which the reactions were performed. The temperature at the end of the reaction was 40°C. The dark reaction at this temperature gave results similar to the light reaction. Therefore, it was not possible to rule out that the enhancement of gas evolution could be caused purely by the increased temperature. No conversion was observed with only commercial TiN, which shows Pd is present in the catalyst and is the active catalysing material in the reaction.

In further work, the heating was addressed using fans and stabilising the temperature before starting the reaction. The dependence on light intensity on the reaction was studied (Figure 34, B). The dark reaction is performed at the same temperature as was caused

by heating in four-light measurement (31°C). The four-lamp and dark reactions are very similar, and the two- lamp reaction was only slightly lower in gas evolution. According to the similarity, it seems that the enhancement is only thermal. The measurement set-up follows the amount of gas formation in the reaction system. It should be verified that the formed gas is hydrogen and not some other gas, for example, water evaporated from the reaction due to the heating.

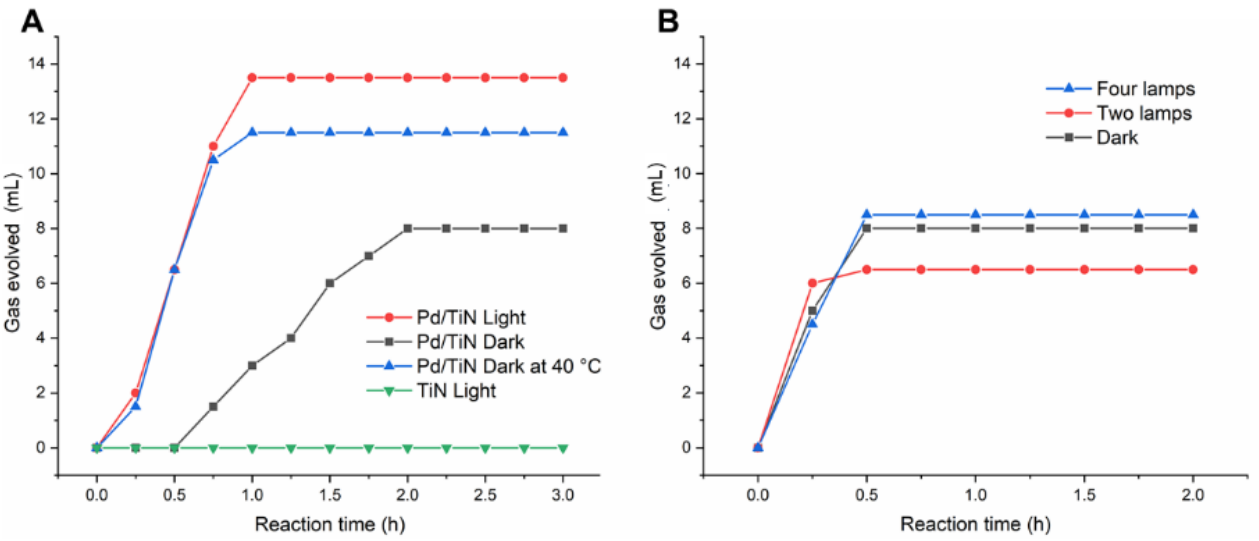

Figure 34. Ammonium borane dehydrogenation. A: Effect of the temperature on the reaction. B: Effect of the light intensity.

3.4. Discussion

Characterisation done with XRD, MP AES and SEM showed Pd clusters were successfully reduced on the surfaces of TiN particles. With 3 % metal loading, the calculated amount of Pd was obtained in the catalyst. This result can be expected to hold to other metal loadings as well.

Water suspension UV-Vis spectrometry showed an absorption peak in 680 nm, which is in agreement with the TiN peak in the previous studies[49,129].The Pd loading causes the

peak to shift to slightly longer wavelengths. DRS showed absorption in the 450 nm region, which is similar to reported by Kaur et al.[113]

The difference in maximum absorption in solid and suspension measurements is unintuitive, and the reason for that is unclear. In literature, the absorption is more often measured from suspensions. However, the medium can affect the absorption peak, and some changes can happen in the water suspension. A future study of reactions with different light wavelengths could designate the best wavelength for the lamp used and give an insight into any dependence of the reaction rate on the wavelength.

The performed catalytical reactions showed no enhancement under light irradiation caused by the plasmonic properties of TiN. To further study the Pd/TiN catalyst, adjustments to the reaction conditions, such as reactant/catalytic metal – ratio, could be optimised. Also, some other reactions known to be catalysed with palladium could be tested.

The reproducibility of the catalytical reactions was poor. In both phenylacetylene and ammonium borane reactions, the differences between single reactions were more significant than the differences between light and dark. Better control of the reaction temperature could give more accurate results.

SEM images showed Pd-islands to cluster. To better the catalyst, the distribution of these islands could be optimised. Uneven distribution of the catalysing metal might cause differences between the reaction batches. The plasmonic response is a property of particles with a size smaller than the incident light wavelength[1]. It can be speculated that the <3 µm size TiN particles used in the catalysts for phenylacetylene hydrogenation were too large to have plasmonic activity. However, then the significant absorption of <3 µm particles should be then explained differently.

A property of TiN nanoparticles that was not taken into account in this study, but could significantly affect the catalyst performance, is the TiN oxidation. Upon exposure to air, a self-passivating layer of TiO_2 forms on the TiN particle surface[112]. Guler et al. studied commercial, 50 nm TiN particles purchased from PlasmaChem, the same size and vendor as used in this study, and report a 1-2 nm TiO_2 layer in water suspended TiN particles[129].

In another study, the effect of TiN particle oxidation on plasmonic properties was studied. Barragan et al. prepared TiN nanoparticles with different N/Ti -ratios and showed that the particles with low nitrogen content were the most oxidised and showed an LSPR peak lower and red-shifted compared to the particles with higher N /Ti -ratio[106]. The nitrogen-deficient particles were identified to contain oxynitride. Annealing of the particles in air was also studied. Already annealing for 1 h in 150 °C lowered the absorption peak. In light of this result, it should be assessed if any changes happen in the Pd/TiN synthesis, especially in the drying step.

The oxidation of the TiN in the prepared catalyst should be studied to better understand the system and its plasmonic properties. DRS and suspension spectrophotometry measurements show only a slight lowering of the absorption in the synthesised catalyst, indicating the plasmonic properties of the material are preserved. The change in absorption can also be caused by Pd loading. This result would suggest that the oxidation of the nanoparticle core is insignificant for the plasmonic properties. However, the oxide layer between TiN and Pd can cause an additional effect on the energy transfer between the plasmonic and catalytic parts of the system.

In their study, Rej et al. suggest the surface layer can be removed from commercial TiN particles by acid treatment[112]. In their work, the Pt/TiN catalyst was prepared and stored in a non-oxidating atmosphere; nonetheless, an oxide layer was observed on TiN. Other research suggests that the oxidation can be reduced by covering formed TiN nanoparticles with a silicon nitride[130] or SiO_2[110] layer. These strategies should also be considered, however is unclear if a similar approach would be possible for commercial TiN particles.

3.5. Conclusions

In this work, a Pd/TiN hybrid catalyst was synthesised. Its plasmonic photocatalytic properties were compared on model reactions in the dark and under light irradiation in phenylacetylene hydrogenation and ammonium borane dehydrogenation. Characterisation with various methods showed the catalyst material to be what was

expected. However, within the span of the work, no catalytic activity enhancement under light irradiation was observed.

Further studies with different reaction parameters or reactions should be done to understand the system better. Further studies of the catalytic reactions should include: 1) assessing more precisely the heating caused by lamps on the reaction system to gain repeatable conditions 2) wavelength dependence study of the enhancement 3) reactions with varying the reactant/metal ratio, and possibly 4) study of a different catalytical reaction to see if the system performs better with some other transformation and avoid problem arising from a specific reaction. Other considerations should include optimising the synthesis of the catalyst to produce high dispersion of Pd on the TiN surfaces and confirming that the TiN oxidation is limited to the surface and does not diminish the optical properties.

References

(1) Aslam, U.; Rao, V. G.; Chavez, S.; Linic, S. Catalytic Conversion of Solar to Chemical Energy on Plasmonic Metal Nanostructures. *Nat. Catal.* **2018**, *1* (9), 656–665. https://doi.org/10.1038/s41929-018-0138-x.

(2) Védrine, J. C. 9 - Concluding Remarks and Challenges of Heterogeneous Catalysis on Metal Oxides. In *Metal Oxides in Heterogeneous Catalysis*; Elsevier Inc, 2018; pp 551–569.

(3) Bhattacharya, C.; Saji, S. E.; Mohan, A.; Madav, V.; Jia, G.; Yin, Z. Sustainable Nanoplasmon-Enhanced Photoredox Reactions: Synthesis, Characterization, and Applications. *Adv. Energy Mater.* **2020**, *10* (40), 1–32. https://doi.org/10.1002/aenm.202002402.

(4) Dekker, F.; Kool, L.; Bunschoten, A.; Velders, A. H.; Saggiomo, V. Syntheses of Gold and Silver Dichroic Nanoparticles; Looking at the Lycurgus Cup Colors. *Chem. Teach. Int.* **2021**, *3* (1), 1–6. https://doi.org/10.1515/cti-2019-0011.

(5) Faraday, M. Experimental Relations o f Gold (and Other Metals) to Light. *Phil. Trans. R. Soc.* **1857**, *147* (0), 145–181.

(6) Awazu, K.; Fujimaki, M.; Rockstuhl, C.; Tominaga, J.; Murakami, H.; Ohki, Y.; Yoshida, N.; Watanabe, T. A Plasmonic Photocatalyst Consisting of Silver Nanoparticles Embedded in Titanium Dioxide. *J. Am. Chem. Soc.* **2008**, *130* (5), 1676–1680.

https://doi.org/10.1021/ja076503n.

(7) Christopher, P.; Xin, H.; Linic, S. Visible-Light-Enhanced Catalytic Oxidation Reactions on Plasmonic Silver Nanostructures. *Nat. Chem.* **2011**, *3* (6), 467–472. https://doi.org/10.1038/nchem.1032.

(8) Naik, G. V.; Kim, J.; Boltasseva, A. Oxides and Nitrides as Alternative Plasmonic Materials in the Optical Range [Invited]. *Opt. Mater. Express* **2011**. https://doi.org/10.1364/ome.1.001090.

(9) Guler, U.; Shalaev, V. M.; Boltasseva, A. Nanoparticle Plasmonics: Going Practical with Transition Metal Nitrides. *Mater. Today* **2015**, *18* (4), 227–237. https://doi.org/10.1016/j.mattod.2014.10.039.

(10) Kim, S.; Kim, J. M.; Park, J. E.; Nam, J. M. Nonnoble-Metal-Based Plasmonic Nanomaterials: Recent Advances and Future Perspectives. *Adv. Mater.* **2018**, *30* (42), 1–24. https://doi.org/10.1002/adma.201704528.

(11) Sytwu, K.; Vadai, M.; Dionne, J. A. Bimetallic Nanostructures: Combining Plasmonic and Catalytic Metals for Photocatalysis. *Adv. Phys. X* **2019**, *4* (1). https://doi.org/10.1080/23746149.2019.1619480.

(12) IUPAC. Compendium of Chemical Terminology, 2nd ed. (the "Gold Book"). Compiled by A. D. McNaught and A. Wilkinson. Blackwell Scientific Publications, Oxford (1997). Online version (2019-) created by S. J. Chalk. ISBN 0-9678550-9-8. https://doi.org/10.1351/goldbook

(13) McCash, E. M. *Surface Chemistry*; Oxford University Press: Oxford, 2001.

(14) Védrine, J. C. 1 - Fundamentals of Heterogeneous Catalysis. In *Metal Oxides in Heterogeneous Catalysis*; Elsevier Inc, 2018; pp 1–41. https://doi.org/10.1016/B978-0-12-811631-9.00001-6.

(15) Nørskov, J. K.; Studt, F.; Abild-Pedersen, F.; Bligaard, T. Heterogeneous Catalysis and a Sustainable Future. In *Fundamental Concepts in Heterogeneous Catalysis*; John Wiley & Sons, Inc: Hoboken, NJ, USA, 2014; pp 1–5.

(16) Anastas, P. T.; Warner, J. C. *Green Chemistry : Theory and Practice*; Oxford University Press: Oxford, 1998.

(17) Rodríguez-Padrón, D.; Puente-Santiago, A. R.; Balu, A. M.; Muñoz-Batista, M. J.; Luque, R. Environmental Catalysis: Present and Future. *ChemCatChem* **2019**, *11* (1), 18–38. https://doi.org/10.1002/cctc.201801248.

(18) Kuwahara, Y.; Yoshimura, Y.; Haematsu, K.; Yamashita, H. Mild Deoxygenation of Sulfoxides over Plasmonic Molybdenum Oxide Hybrid with Dramatic Activity Enhancement under Visible Light. *J. Am. Chem. Soc.* **2018**, *140* (29), 9203–9210. https://doi.org/10.1021/jacs.8b04711.

(19) Swearer, D. F.; Robatjazi, H.; Martirez, J. M. P.; Zhang, M.; Zhou, L.; Carter, E. A.; Nordlander, P.; Halas, N. J. Plasmonic Photocatalysis of Nitrous Oxide into N2 and O2 Using Aluminum-Iridium Antenna-Reactor Nanoparticles. *ACS Nano* **2019**, *13* (7), 8076–8086. https://doi.org/10.1021/acsnano.9b02924.

(20) Zhang, Y.; He, S.; Guo, W.; Hu, Y.; Huang, J.; Mulcahy, J. R.; Wei, W. D. Surface-Plasmon-Driven Hot Electron Photochemistry. *Chem. Rev.* **2018**, *118* (6), 2927–2954.

https://doi.org/10.1021/acs.chemrev.7b00430.

(21) Polshettiwar, V.; Varma, R. S. Green Chemistry by Nano-Catalysis. *Green Chem.* **2010**, *12* (5), 743–775. https://doi.org/10.1039/b921171c.

(22) Hunt, A. J.; Farmer, T. J. Chapter 1 Elemental Sustainability for Catalysis. In *Sustainable Catalysis: With Non-endangered Metals, Part 1*; The Royal Society of Chemistry, 2016; pp 1–14. https://doi.org/10.1039/9781782622116-00001.

(23) Zhou, L.; Martirez, J. M. P.; Finzel, J.; Zhang, C.; Swearer, D. F.; Tian, S.; Robatjazi, H.; Lou, M.; Dong, L.; Henderson, L.; Christopher, P.; Carter, E. A.; Nordlander, P.; Halas, N. J. Light-Driven Methane Dry Reforming with Single Atomic Site Antenna-Reactor Plasmonic Photocatalysts. *Nat. Energy* **2020**, *5* (1), 61–70. https://doi.org/10.1038/s41560-019-0517-9.

(24) Cui, J.; Li, Y.; Liu, L.; Chen, L.; Xu, J.; Ma, J.; Fang, G.; Zhu, E.; Wu, H.; Zhao, L.; Wang, L.; Huang, Y. Near-Infrared Plasmonic-Enhanced Solar Energy Harvest for Highly Efficient Photocatalytic Reactions. *Nano Lett.* **2015**, *15* (10), 6295–6301. https://doi.org/10.1021/acs.nanolett.5b00950.

(25) Wu, S.; Wu, S.; Sun, Y. Light-Driven Dry Reforming of Methane on Metal Catalysts. *Sol. RRL* **2020**, *2000507*, 1–12. https://doi.org/10.1002/solr.202000507.

(26) Bullock, R. M.; Che, J. G.; Gagliardi, L.; Chiri, P. J.; Farh, O. K.; Hendo, C. H.; Jone, C. W.; Keit, J. A.; Klosin, J.; Mintee, S. D.; Morri, R. H.; Radosevic, A. T.; Rauchfus, T. B.; Strotma, N. A.; Vojvodic, A.; War, T. R.; Yan, J. Y.; Surendranath, Y. Using Nature's Blueprint to Expand Catalysis with Earth-Abundant Metals. *Science (80-.).* **2020**, *369* (6505). https://doi.org/10.1126/science.abc3183.

(27) Jowitt, S. M.; Mudd, G. M.; Thompson, J. F. H. Future Availability of Non-Renewable Metal Resources and the Influence of Environmental, Social, and Governance Conflicts on Metal Production. *Commun. Earth Environ.* **2020**, *1* (1), 1–8. https://doi.org/10.1038/s43247-020-0011-0.

(28) Henckens, M. L. C. M.; Driessen, P. P. J.; Worrell, E. Metal Scarcity and Sustainability, Analyzing the Necessity to Reduce the Extraction of Scarce Metals. *Resour. Conserv. Recycl.* **2014**, *93*, 1–8. https://doi.org/10.1016/j.resconrec.2014.09.012.

(29) Zecchina, A.; Califano, S. Photocatalysis; John Wiley & Sons, Inc: Hoboken, New Jersey, 2017; pp 243–268. https://doi.org/10.1002/9781119181286.ch7.

(30) Zhan, C.; Moskovits, M.; Tian, Z. Q. Recent Progress and Prospects in Plasmon-Mediated Chemical Reaction. *Matter* **2020**, *3* (1), 42–56. https://doi.org/10.1016/j.matt.2020.03.019.

(31) Maier, S. A. Localized Surface Plasmons. In *Plasmonics: Fundamentals and Applications*; Springer US: New York, NY, 2007; pp 65–88. https://doi.org/10.1007/0-387-37825-1_5.

(32) Linic, S.; Chavez, S.; Elias, R. Flow and Extraction of Energy and Charge Carriers in Hybrid Plasmonic Nanostructures. *Nat. Mater.* **2021**, *15* (2). https://doi.org/10.1038/s41563-020-00858-4.

(33) Lee, K. S.; El-Sayed, M. A. Gold and Silver Nanoparticles in Sensing and Imaging: Sensitivity of Plasmon Response to Size, Shape, and Metal Composition. *J. Phys. Chem. B* **2006**, *110* (39), 19220–19225. https://doi.org/10.1021/jp062536y.

(34) Ringe, E. Shapes, Plasmonic Properties, and Reactivity of Magnesium Nanoparticles. *J. Phys. Chem. C* **2020**, *124* (29), 15665–15679. https://doi.org/10.1021/acs.jpcc.0c03871.

(35) Mcmahon, J. M.; Schatz, G. C.; Gray, S. K. Plasmonics in the Ultraviolet with the Poor Metals. **2013**, 5415–5423. https://doi.org/10.1039/c3cp43856b.

(36) Agrawal, A.; Cho, S. H.; Zandi, O.; Ghosh, S.; Johns, R. W.; Milliron, D. J. Localized Surface Plasmon Resonance in Semiconductor Nanocrystals. *Chem. Rev.* **2018**, *118* (6), 3121–3207. https://doi.org/10.1021/acs.chemrev.7b00613.

(37) Sanz, J. M.; Ortiz, D.; Alcaraz De La Osa, R.; Saiz, J. M.; González, F.; Brown, A. S.; Losurdo, M.; Everitt, H. O.; Moreno, F. UV Plasmonic Behavior of Various Metal Nanoparticles in the Near- and Far-Field Regimes: Geometry and Substrate Effects. *J. Phys. Chem. C* **2013**, *117* (38), 19606–19615. https://doi.org/10.1021/jp405773p.

(38) Agrawal, A.; Cho, S. H.; Zandi, O.; Ghosh, S.; Johns, R. W.; Milliron, D. J. Localized Surface Plasmon Resonance in Semiconductor Nanocrystals. **2018**. https://doi.org/10.1021/acs.chemrev.7b00613.

(39) Luther, J. M.; Jain, P. K.; Ewers, T.; Alivisatos, A. P. Localized Surface Plasmon Resonances Arising from Free Carriers in Doped Quantum Dots. *Nat. Mater.* **2011**, *10* (5), 361–366. https://doi.org/10.1038/nmat3004.

(40) Cheng, H.; Wen, M.; Ma, X.; Kuwahara, Y.; Mori, K.; Dai, Y.; Huang, B.; Yamashita, H. Hydrogen Doped Metal Oxide Semiconductors with Exceptional and Tunable Localized Surface Plasmon Resonances. *J. Am. Chem. Soc.* **2016**, *138* (29), 9316–9324. https://doi.org/10.1021/jacs.6b05396.

(41) Naik, G. V; Schroeder, J. L.; Ni, X.; Kildishev, A. V; Sands, T. D.; Boltasseva, A. Titanium Nitride as a Plasmonic Material for Visible and Near-Infrared Wavelengths. *Opt. Mater. Express* **2012**, *2* (4), 478–489. https://doi.org/10.1364/OME.2.000478.

(42) Mcmahon, M. D.; Lopez, R.; Meyer, H. M.; Feldman, L. C.; Haglund, R. F. Rapid Tarnishing of Silver Nanoparticles in Ambient Laboratory Air. *Appl. Phys. B Lasers Opt.* **2005**, *80* (7), 915–921. https://doi.org/10.1007/s00340-005-1793-6.

(43) Kale, M. J.; Avanesian, T.; Christopher, P. Direct Photocatalysis by Plasmonic Nanostructures. *ACS Catal.* **2014**, *4* (1), 116–128. https://doi.org/10.1021/cs400993w.

(44) Adleman, J. R.; Boyd, D. A.; Goodwin, D. G.; Psaltis, D. Heterogenous Catalysis Mediated by Plasmon Heating. *Nano Lett.* **2009**, *9* (12), 4417–4423. https://doi.org/10.1021/nl902711n.

(45) Naldoni, A.; Kudyshev, Z. A.; Mascaretti, L.; Sarmah, S. P.; Rej, S.; Froning, J. P.; Tomanec, O.; Yoo, J. E.; Wang, D.; Kment, Š.; Montini, T.; Fornasiero, P.; Shalaev, V. M.; Schmuki, P.; Boltasseva, A.; Zbořil, R. Solar Thermoplasmonic Nanofurnace for High-Temperature Heterogeneous Catalysis. *Nano Lett.* **2020**, *20* (5), 3663–3672. https://doi.org/10.1021/acs.nanolett.0c00594.

(46) Boyd, D. A.; Greengard, L.; Brongersma, M.; El-Naggar, M. Y.; Goodwin, D. G. Plasmon-Assisted Chemical Vapor Deposition. *Nano Lett.* **2006**, *6* (11), 2592–2597. https://doi.org/10.1021/nl062061m.

(47) He, W.; Ai, K.; Jiang, C.; Li, Y.; Song, X.; Lu, L. Plasmonic Titanium Nitride Nanoparticles for in Vivo Photoacoustic Tomography Imaging and Photothermal Cancer Therapy. *Biomaterials* **2017**, *132*, 37–47. https://doi.org/10.1016/j.biomaterials.2017.04.007.

(48) Zhang, X.; Zu, H.; Guo, Y.; Liu, Q.; Liu, Z.; Hu, C. Morphology-Controlled Synthesis of Molybdenum Oxide with Tunable Plasmon Absorption for Photothermal Therapy of Cancer. *ChemNanoMat* **2020**, *6* (9), 1407–1416. https://doi.org/10.1002/cnma.202000311.

(49) Kaur, M.; Ishii, S.; Shinde, S. L.; Nagao, T. All-Ceramic Microfibrous Solar Steam Generator: TiN Plasmonic Nanoparticle-Loaded Transparent Microfibers. *ACS Sustain. Chem. Eng.* **2017**, *5* (10), 8523–8528. https://doi.org/10.1021/acssuschemeng.7b02089.

(50) Sivan, Y.; Un, I. W.; Dubi, Y. Assistance of Metal Nanoparticles in Photocatalysis-Nothing More than a Classical Heat Source. *Faraday Discuss.* **2019**, *214*, 215–233. https://doi.org/10.1039/c8fd00147b.

(51) Baffou, G.; Bordacchini, I.; Baldi, A. Simple Experimental Procedures to Distinguish Photothermal from Hot-Carrier Processes in Plasmonics. *Light Sci. Appl.* **2020**. https://doi.org/10.1038/s41377-020-00345-0.

(52) Nørskov, J. K.; Studt, F.; Abild-Pedersen, F.; Bligaard, T. The Electronic Factor in Heterogeneous Catalysis. In *Fundamental Concepts in Heterogeneous Catalysis*; John Wiley & Sons, Inc: Hoboken, NJ, USA, 2014; pp 114–137. https://doi.org/10.1002/9781118892114.ch8.

(53) Li, C.; Yang, W.; Liu, L.; Sun, W.; Li, Q. In Situ Growth of TiO2 on TiN Nanoparticles for Non-Noble-Metal Plasmonic Photocatalysis. *RSC Adv.* **2016**, *6* (76), 72659–72669. https://doi.org/10.1039/c6ra15435b.

(54) Habib, A.; Zhu, X.; Fong, S.; Yanik, A. A. Active Plasmonic Nanoantenna: An Emerging Toolbox from Photonics to Neuroscience. *Nanophotonics* **2020**, *9* (12), 3805–3829. https://doi.org/10.1515/nanoph-2020-0275.

(55) Swearer, D. F.; Zhao, H.; Zhou, L.; Zhang, C.; Robatjazi, H.; Martirez, J. M. P.; Krauter, C. M.; Yazdi, S.; McClain, M. J.; Ringe, E.; Carter, E. A.; Nordlander, P.; Halas, N. J. Heterometallic Antenna-Reactor Complexes for Photocatalysis. *Proc. Natl. Acad. Sci. U. S. A.* **2016**, *113* (32), 8916–8920. https://doi.org/10.1073/pnas.1609769113.

(56) Zhang, C.; Zhao, H.; Zhou, L.; Schlather, A. E.; Dong, L.; McClain, M. J.; Swearer, D. F.; Nordlander, P.; Halas, N. J. Al-Pd Nanodisk Heterodimers as Antenna-Reactor Photocatalysts. *Nano Lett.* **2016**, *16* (10), 6677–6682. https://doi.org/10.1021/acs.nanolett.6b03582.

(57) Araujo, T. P.; Quiroz, J.; Barbosa, E. C. M.; Camargo, P. H. C. Understanding Plasmonic Catalysis with Controlled Nanomaterials Based on Catalytic and Plasmonic Metals. *Curr. Opin. Colloid Interface Sci.* **2019**, *39*, 110–122. https://doi.org/10.1016/j.cocis.2019.01.014.

(58) Aslam, U.; Chavez, S.; Linic, S. Controlling Energy Flow in Multimetallic Nanostructures for Plasmonic Catalysis. *Nat. Nanotechnol.* **2017**, *12* (10), 1000–1005. https://doi.org/10.1038/nnano.2017.131.

(59) Chavez, S.; Aslam, U.; Linic, S. Design Principles for Directing Energy and Energetic Charge Flow in Multicomponent Plasmonic Nanostructures. *ACS Energy Lett.* **2018**, *3* (7), 1590–1596. https://doi.org/10.1021/acsenergylett.8b00841.

(60) Chavez, S.; Rao, V. G.; Linic, S. Unearthing the Factors Governing Site Specific Rates of Electronic Excitations in Multicomponent Plasmonic Systems and Catalysts. *Faraday Discuss.* **2019**, *214*, 441–453. https://doi.org/10.1039/c8fd00143j.

(61) Spetter, D.; Tahir, M. N.; Hilgert, J.; Khan, I.; Qurashi, A.; Lu, H.; Weidner, T.; Tremel, W. Solvothermal Synthesis of Molybdenum-Tungsten Oxides and Their Application for Photoelectrochemical Water Splitting. *ACS Sustain. Chem. Eng.* **2018**, *6* (10), 12641–12649. https://doi.org/10.1021/acssuschemeng.8b01370.

(62) Deng, S.; Zhang, B.; Choo, P.; Smeets, P. J. M.; Odom, T. W. Plasmonic Photoelectrocatalysis in Copper–Platinum Core–Shell Nanoparticle Lattices. *Nano Lett.* **2021**. https://doi.org/10.1021/acs.nanolett.0c05029.

(63) Gawande, M. B.; Goswami, A.; Felpin, F. X.; Asefa, T.; Huang, X.; Silva, R.; Zou, X.; Zboril, R.; Varma, R. S. Cu and Cu-Based Nanoparticles: Synthesis and Applications in Catalysis. *Chem. Rev.* **2016**, *116* (6), 3722–3811. https://doi.org/10.1021/acs.chemrev.5b00482.

(64) Popok, V. N.; Novikov, S. M.; Lebedinskij, Y. Y.; Markeev, A. M.; Andreev, A. A.; Trunkin, I. N.; Arsenin, A. V.; Volkov, V. S. Gas-Aggregated Copper Nanoparticles with Long-Term Plasmon Resonance Stability. *Plasmonics* **2020**, No. I. https://doi.org/10.1007/s11468-020-01287-4.

(65) Guo, X.; Hao, C.; Jin, G.; Zhu, H. Y.; Guo, X. Y. Copper Nanoparticles on Graphene Support: An Efficient Photocatalyst for Coupling of Nitroaromatics in Visible Light. *Angew. Chemie - Int. Ed.* **2014**, *53* (7), 1973–1977. https://doi.org/10.1002/anie.201309482.

(66) Marimuthu, A.; Zhang, J.; Linic, S. Tuning Selectivity in Propylene Epoxidation by Plasmon Mediated Photo-Switching of Cu Oxidation State. *Science (80-.).* **2013**, *340* (6127), 1590–1593. https://doi.org/10.1126/science.1231631.

(67) Wang, Z. jun; Song, H.; Pang, H.; Ning, Y.; Dao, T. D.; Wang, Z.; Chen, H.; Weng, Y.; Fu, Q.; Nagao, T.; Fang, Y.; Ye, J. Photo-Assisted Methanol Synthesis via CO2 Reduction under Ambient Pressure over Plasmonic Cu/ZnO Catalysts. *Appl. Catal. B Environ.* **2019**, *250* (February), 10–16. https://doi.org/10.1016/j.apcatb.2019.03.003.

(68) Xu, Y.; Zhang, H.; Song, J.; Wang, D.; Gu, X. Boosting the On-Demand Hydrogen Generation from Aqueous Ammonia Borane by the Visible-Light-Driven Synergistic Electron Effect in Antenna-Reactor-Type Catalysts with Plasmonic Copper Spheres and Noble-Metal-Free Nanoparticles. *Chem. Eng. J.* **2020**, *401* (April), 126068. https://doi.org/10.1016/j.cej.2020.126068.

(69) Yaroshevsky, A. A. Abundances of Chemical Elements in the Earth's Crust. *Geochemistry Int.* **2006**, *44* (1), 48–55. https://doi.org/10.1134/S001670290601006X.

(70) Gerard, D.; Gray, S. K. Aluminium Plasmonics. *J. Phys. D. Appl. Phys.* **2015**, *48* (18). https://doi.org/10.1088/0022-3727/48/18/184001.

(71) Knight, M. W.; King, N. S.; Liu, L.; Everitt, H. O.; Nordlander, P.; Halas, N. J. Aluminum for Plasmonics. *ACS Nano* **2014**, *8* (1), 834–840. https://doi.org/10.1021/nn405495q.

(72) Langhammer, C.; Schwind, M.; Kasemo, B.; Zorić, I. Localized Surface Plasmon Resonances in Aluminum Nanodisks. *Nano Lett.* **2008**, *8* (5), 1461–1471. https://doi.org/10.1021/nl080453i.

(73) Haber, J. A.; Buhro, W. E. Kinetic Instability of Nanocrystalline Aluminum Prepared by Chemical Synthesis; Facile Room-Temperature Grain Growth. *J. Am. Chem. Soc.* **1998**, *120* (42), 10847–10855. https://doi.org/10.1021/ja981972y.

(74) McClain, M. J.; Schlather, A. E.; Ringe, E.; King, N. S.; Liu, L.; Manjavacas, A.; Knight, M.

W.; Kumar, I.; Whitmire, K. H.; Everitt, H. O.; Nordlander, P.; Halas, N. J. Aluminum Nanocrystals. *Nano Lett.* **2015**, *15* (4), 2751–2755. https://doi.org/10.1021/acs.nanolett.5b00614.

(75) Yang, S.; Lu, S.; Li, Y.; Yu, H.; He, L.; Sun, T.; Yang, B.; Liu, K. Poly(Ethylene Oxide) Mediated Synthesis of Sub-100-Nm Aluminum Nanocrystals for Deep Ultraviolet Plasmonic Nanomaterials. *CCS Chem.* **2020**, *2* (4), 516–526. https://doi.org/10.31635/ccschem.020.202000141.

(76) Jacobson, C. R.; Solti, D.; Renard, D.; Yuan, L.; Lou, M.; Halas, N. J. Shining Light on Aluminum Nanoparticle Synthesis. *Acc. Chem. Res.* **2020**, *53* (9), 2020–2030. https://doi.org/10.1021/acs.accounts.0c00419.

(77) Robatjazi, H.; Lou, M.; Clark, B. D.; Jacobson, C. R.; Swearer, D. F.; Nordlander, P.; Halas, N. J. Site-Selective Nanoreactor Deposition on Photocatalytic Al Nanocubes. *Nano Lett.* **2020**, *20* (6), 4550–4557. https://doi.org/10.1021/acs.nanolett.0c01405.

(78) Robatjazi, H.; Bao, J. L.; Zhang, M.; Zhou, L.; Christopher, P.; Carter, E. A.; Nordlander, P.; Halas, N. J. Plasmon-Driven Carbon–Fluorine (C(Sp 3)–F) Bond Activation with Mechanistic Insights into Hot-Carrier-Mediated Pathways. *Nat. Catal.* **2020**, *3* (7), 564–573. https://doi.org/10.1038/s41929-020-0466-5.

(79) Robatjazi, H.; Zhao, H.; Swearer, D. F.; Hogan, N. J.; Zhou, L.; Alabastri, A.; McClain, M. J.; Nordlander, P.; Halas, N. J. Plasmon-Induced Selective Carbon Dioxide Conversion on Earth-Abundant Aluminum-Cuprous Oxide Antenna-Reactor Nanoparticles. *Nat. Commun.* **2017**, *8* (1), 1–9. https://doi.org/10.1038/s41467-017-00055-z.

(80) Swearer, D. F.; Leary, R. K.; Newell, R.; Yazdi, S.; Robatjazi, H.; Zhang, Y.; Renard, D.; Nordlander, P.; Midgley, P. A.; Halas, N. J.; Ringe, E. Transition-Metal Decorated Aluminum Nanocrystals. *ACS Nano* **2017**, *11* (10), 10281–10288. https://doi.org/10.1021/acsnano.7b04960.

(81) Hao, Q.; Wang, C.; Huang, H.; Li, W.; Du, D.; Han, D.; Qiu, T.; Chu, P. K. Aluminum Plasmonic Photocatalysis. *Sci. Rep.* **2015**, *5*, 1–7. https://doi.org/10.1038/srep15288.

(82) Piot, A.; Earl, S. K.; Ng, C.; Dligatch, S.; Roberts, A.; Davis, T. J.; Gómez, D. E. Collective Excitation of Plasmonic Hot-Spots for Enhanced Hot Charge Carrier Transfer in Metal/Semiconductor Contacts. *Nanoscale* **2015**, *7* (18), 8294–8298. https://doi.org/10.1039/c5nr01592h.

(83) Gutiérrez, Y.; Giangregorio, M. M.; Palumbo, F.; González, F.; Brown, A. S.; Moreno, F.; Losurdo, M. Sustainable and Tunable Mg/Mgo Plasmon-Catalytic Platform for the Grand Challenge of Sf6 Environmental Remediation. *Nano Lett.* **2020**, *20* (5), 3352–3360. https://doi.org/10.1021/acs.nanolett.0c00244.

(84) Sterl, F.; Strohfeldt, N.; Walter, R.; Griessen, R.; Tittl, A.; Giessen, H. Magnesium as Novel Material for Active Plasmonics in the Visible Wavelength Range. *Nano Lett.* **2015**, *15* (12), 7949–7955. https://doi.org/10.1021/acs.nanolett.5b03029.

(85) Duan, X.; Kamin, S.; Liu, N. Dynamic Plasmonic Colour Display. *Nat. Commun.* **2017**, *8*, 1–9. https://doi.org/10.1038/ncomms14606.

(86) Asselin, J.; Boukouvala, C.; Wu, Y.; Hopper, E. R.; Collins, S. M.; Biggins, J. S.; Ringe, E. Decoration of Plasmonic Mg Nanoparticles by Partial Galvanic Replacement. *J. Chem. Phys.* **2019**, *151* (24). https://doi.org/10.1063/1.5131703.

(87) Xia, X.; Wang, Y.; Ruditskiy, A.; Xia, Y. 25th Anniversary Article: Galvanic Replacement: A Simple and Versatile Route to Hollow Nanostructures with Tunable and Well-Controlled Properties. *Adv. Mater.* **2013**, *25* (44), 6313–6333. https://doi.org/10.1002/adma.201302820.

(88) Cheng, H.; Qian, X.; Kuwahara, Y.; Mori, K.; Yamashita, H. A Plasmonic Molybdenum Oxide Hybrid with Reversible Tunability for Visible-Light-Enhanced Catalytic Reactions. *Adv. Mater.* **2015**, *27* (31), 4616–4621. https://doi.org/10.1002/adma.201501172.

(89) Yin, H.; Kuwahara, Y.; Mori, K.; Louis, C.; Yamashita, H. Properties, Fabrication and Applications of Plasmonic Semiconductor Nanocrystals. *Catal. Sci. Technol.* **2020**, *10* (13), 4141–4163. https://doi.org/10.1039/c9cy02511a.

(90) Yin, H.; Kuwahara, Y.; Mori, K.; Che, M.; Yamashita, H. Plasmonic Ru/Hydrogen Molybdenum Bronzes with Tunable Oxygen Vacancies for Light-Driven Reduction of: P - Nitrophenol. *J. Mater. Chem. A* **2019**, *7* (8), 3783–3789. https://doi.org/10.1039/c8ta11604k.

(91) Yin, H.; Kuwahara, Y.; Mori, K.; Yamashita, H. RuPd Alloy Nanoparticles Supported on Plasmonic HxMoO3–y for Efficient Photocatalytic Reduction of p-Nitrophenol. *Eur. J. Inorg. Chem.* **2019**, *2019* (33), 3745–3752. https://doi.org/10.1002/ejic.201900801.

(92) Zhang, Q.; Yang, Z.; Chen, X.; Ning, S.; Qi, Y.; Liu, L.; Ye, J. Plasmon-Enhanced CO Selective Oxidation in H2 over Pt Nanoclusters Supported on Metallic Molybdenum Dioxide Nanocrystals. *Adv. Mater. Interfaces* **2020**, *7* (24), 1–8. https://doi.org/10.1002/admi.202001657.

(93) Xi, G.; Ouyang, S.; Li, P.; Ye, J.; Ma, Q.; Su, N.; Bai, H.; Wang, C. Ultrathin W 18O 49 Nanowires with Diameters below 1 Nm: Synthesis, near-Infrared Absorption, Photoluminescence, and Photochemical Reduction of Carbon Dioxide. *Angew. Chemie - Int. Ed.* **2012**, *51* (10), 2395–2399. https://doi.org/10.1002/anie.201107681.

(94) Li, J.; Chen, G.; Yan, J.; Huang, B.; Cheng, H.; Lou, Z.; Li, B. Solar-Driven Plasmonic Tungsten Oxides as Catalyst Enhancing Ethanol Dehydration for Highly Selective Ethylene Production. *Appl. Catal. B Environ.* **2020**, *264* (December 2019), 118517. https://doi.org/10.1016/j.apcatb.2019.118517.

(95) Song, J.; Huang, Z. F.; Pan, L.; Zou, J. J.; Zhang, X.; Wang, L. Oxygen-Deficient Tungsten Oxide as Versatile and Efficient Hydrogenation Catalyst. *ACS Catal.* **2015**, *5* (11), 6594–6599. https://doi.org/10.1021/acscatal.5b01522.

(96) Lou, Z.; Gu, Q.; Liao, Y.; Yu, S.; Xue, C. Promoting Pd-Catalyzed Suzuki Coupling Reactions through near-Infrared Plasmon Excitation of WO3-x Nanowires. *Appl. Catal. B Environ.* **2016**, *184*, 258–263. https://doi.org/10.1016/j.apcatb.2015.11.037.

(97) Lou, Y.; He, J.; Liu, G.; Qi, S.; Cheng, L.; Chen, J.; Zhao, Y.; Zhu, J. J. Efficient Hydrogen Evolution from the Hydrolysis of Ammonia Borane Using Bilateral-like WO3-: X Nanorods Coupled with Ni2P Nanoparticles. *Chem. Commun.* **2018**, *54* (48), 6188–6191. https://doi.org/10.1039/c8cc03502d.

(98) Yin, H.; Kuwahara, Y.; Mori, K.; Cheng, H.; Wen, M.; Huo, Y.; Yamashita, H. Localized Surface Plasmon Resonances in Plasmonic Molybdenum Tungsten Oxide Hybrid for Visible-Light-Enhanced Catalytic Reaction. *J. Phys. Chem. C* **2017**, *121* (42), 23531–23540. https://doi.org/10.1021/acs.jpcc.7b08403.

(99) Yin, H.; Kuwahara, Y.; Mori, K.; Yamashita, H. Plasmonic Metal/Mo:XW1- XO3- y for Visible-Light-Enhanced H2 Production from Ammonia Borane. *J. Mater. Chem. A* **2018**, *6* (23), 10932–10938. https://doi.org/10.1039/c8ta03125h.

(100) Chakrabarti, D. J.; Laughlin, D. E. Cu-S Provisional The Cu-S (Copper-Sulfur) System Equilibrium Diagram. *Bull. Alloy Phase Diagrams* **1983**, *4* (3), 254–271.

(101) Xie, Y.; Carbone, L.; Nobile, C.; Grillo, V.; D'Agostino, S.; Della Sala, F.; Giannini, C.; Altamura, D.; Oelsner, C.; Kryschi, C.; Cozzoli, P. D. Metallic-like Stoichiometric Copper Sulfide Nanocrystals: Phase- and Shape-Selective Synthesis, near-Infrared Surface Plasmon Resonance Properties, and Their Modeling. *ACS Nano* **2013**, *7* (8), 7352–7369. https://doi.org/10.1021/nn403035s.

(102) Han, T.; Nag, A.; Chandra Mukhopadhyay, S.; Xu, Y. Carbon Nanotubes and Its Gas-Sensing Applications: A Review. *Sensors and Actuators, A: Physical*. Elsevier B.V. June 1, 2019, pp 107–143. https://doi.org/10.1016/j.sna.2019.03.053.

(103) Xu, W.; Liu, H.; Zhou, D.; Chen, X.; Ding, N.; Song, H.; Ågren, H. Localized Surface Plasmon Resonances in Self-Doped Copper Chalcogenide Binary Nanocrystals and Their Emerging Applications. *Nano Today* **2020**, *33*. https://doi.org/10.1016/j.nantod.2020.100892.

(104) Liu, P. H.; Wen, M.; Tan, C. S.; Navlani-García, M.; Kuwahara, Y.; Mori, K.; Yamashita, H.; Chen, L. J. Surface Plasmon Resonance Enhancement of Production of H2 from Ammonia Borane Solution with Tunable Cu2−xS Nanowires Decorated by Pd Nanoparticles. *Nano Energy* **2017**, *31* (November 2016), 57–63. https://doi.org/10.1016/j.nanoen.2016.10.064.

(105) Wakabayashi, H.; Saito, Y.; Takeuchi, K.; Mogami, T.; Kunio, T. A Dual-Metal Gate CMOS Technology Using Nitrogen-Concentration-Controlled TiNx Film. *IEEE Trans. Electron Devices* **2001**, *48* (10), 2363–2369. https://doi.org/10.1109/16.954478.

(106) Alvarez Barragan, A.; Ilawe, N. V.; Zhong, L.; Wong, B. M.; Mangolini, L. A Non-Thermal Plasma Route to Plasmonic TiN Nanoparticles. *J. Phys. Chem. C* **2017**, *121* (4), 2316–2322. https://doi.org/10.1021/acs.jpcc.6b08910.

(107) Karaballi, R. A.; Monfared, Y. E.; Dasog, M. Overview of Synthetic Methods to Prepare Plasmonic Transition-Metal Nitride Nanoparticles. **2020**, 8499–8505. https://doi.org/10.1002/chem.201905217.

(108) Naik, G. V; Kim, J.; Boltasseva, A. Oxides and Nitrides as Alternative Plasmonic Materials in the Optical Range [Invited]. **2011**, *1* (6), 1090–1099.

(109) Lalisse, A.; Tessier, G.; Plain, J.; Baffou, G. Plasmonic Efficiencies of Nanoparticles Made of Metal Nitrides (TiN, ZrN) Compared with Gold. *Sci. Rep.* **2016**, *6* (November), 1–10. https://doi.org/10.1038/srep38647.

(110) Gschwend, P. M.; Conti, S.; Kaech, A.; Maake, C.; Pratsinis, S. E. Silica-Coated TiN Particles for Killing Cancer Cells. *ACS Appl. Mater. Interfaces* **2019**. https://doi.org/10.1021/acsami.9b07239.

(111) Kumar, M.; Umezawa, N.; Ishii, S.; Nagao, T. Examining the Performance of Refractory Conductive Ceramics as Plasmonic Materials: A Theoretical Approach. *ACS Photonics* **2016**, *3* (1), 43–50. https://doi.org/10.1021/acsphotonics.5b00409.

(112) Rej, S.; Mascaretti, L.; Santiago, E. Y.; Tomanec, O.; Kment, Š.; Wang, Z.; Zbořil, R.;

Fornasiero, P.; Govorov, A. O.; Naldoni, A. Determining Plasmonic Hot Electrons and Photothermal Effects during H2 Evolution with TiN-Pt Nanohybrids. *ACS Catal.* **2020**, *10* (9), 5261–5271. https://doi.org/10.1021/acscatal.0c00343.

(113) Kaur, M.; Shinde, S. L.; Ishii, S.; Jevasuwan, W.; Fukata, N.; Yu, M. W.; Li, Y.; Ye, J.; Nagao, T. Marimo-Bead-Supported Core-Shell Nanocomposites of Titanium Nitride and Chromium-Doped Titanium Dioxide as a Highly Efficient Water-Floatable Green Photocatalyst. *ACS Appl. Mater. Interfaces* **2020**, *12* (28), 31327–31339. https://doi.org/10.1021/acsami.0c03781.

(114) Takeda, K.; Yamaguchi, A.; Cho, Y.; Anjaneyulu, O.; Fujita, T.; Abe, H.; Miyauchi, M. Metal Carbide as A Light-Harvesting and Anticoking Catalysis Support for Dry Reforming of Methane. *Glob. Challenges* **2020**, *4* (1), 1900067. https://doi.org/10.1002/gch2.201900067.

(115) Anjaneyulu, O.; Takeda, K.; Ishii, S.; Ueda, S.; Nagao, T.; Xiaobo, P.; Fujita, T.; Miyauchi, M.; Abe, H. Light-Promoted Conversion of Greenhouse Gases over Plasmonic Metal-Carbide Nanocomposite Catalysts. *Mater. Chem. Front.* **2018**, *2* (3), 580–584. https://doi.org/10.1039/C7QM00569E.

(116) Fan, J.; Du, H.; Zhao, Y.; Wang, Q.; Liu, Y.; Li, D.; Feng, J. Recent Progress on Rational Design of Bimetallic Pd Based Catalysts and Their Advanced Catalysis. *ACS Catal.* **2020**, *10* (22), 13560–13583. https://doi.org/10.1021/acscatal.0c03280.

(117) Cardoso, M. B. T.; Lewis, E.; Castro, P. S.; Dantas, L. M. F.; De Oliveira, C. C. S.; Bertotti, M.; Haigh, S. J.; Camargo, P. H. C. A Facile Strategy to Support Palladium Nanoparticles on Carbon Nanotubes, Employing Polyvinylpyrrolidone as a Surface Modifier. *Eur. J. Inorg. Chem.* **2014**, No. 9, 1439–1445. https://doi.org/10.1002/ejic.201301585.

(118) Soares, J. A. N. T. Introduction to Optical Characterization of Materials. In *Practical Materials Characterization*; Sardela, M., Ed.; Springer New York: New York, NY, 2014; pp 43–92. https://doi.org/10.1007/978-1-4614-9281-8_2.

(119) Leng, Y. *Materials Characterization : Introduction to Microscopic and Spectroscopic Methods*; John Wiley & Sons, Incorporated: Weinheim, GERMANY, 2013.

(120) Bindell, J. B. SEM Scanning Electron Microscopy. In *Encyclopedia of materials characterization : surfaces, interfaces, thin films*; Brundle, C. R., Evans, C. A., Fitzpatrick, L. E., Wilson, S., Eds.; Materials characterization series; Butterworth-Heinemann: Boston (MA), 1992; pp 70–83.

(121) Lajunen, L. H. J.; Perämäki, P. Plasma Atomic Emission Spectrometry. In *Spectrochemical analysis by atomic absorption and emission, 2nd edition*; Royal Society of Chemistry, 2007.

(122) Tissue, B. M. Atomic Spectrometry. In *Basics of Analytical Chemistry and Chemical Equilibria*; John Wiley & Sons, Inc: Hoboken, NJ, USA, 2013; pp 340–366.

(123) Sardela, M. R. X-Ray Diffraction and Reflectivity. In *Practical Materials Characterization*; Sardela, M., Ed.; Springer New York: New York, NY, 2014; pp 1–41. https://doi.org/10.1007/978-1-4614-9281-8_1.

(124) Toney, M. XRD X-Ray Diffraction. In *Encyclopedia of materials characterization : surfaces, interfaces, thin films*; Brundle, C. R., Evans, C. A., Fitzpatrick, L. E., Wilson, S.,

Eds.; Materials characterization series; Butterworth-Heinemann: Boston (MA), 1992.

(125) Weerachawanasak, P.; Mekasuwandumrong, O.; Arai, M.; Fujita, S. I.; Praserthdam, P.; Panpranot, J. Effect of Strong Metal-Support Interaction on the Catalytic Performance of Pd/TiO2 in the Liquid-Phase Semihydrogenation of Phenylacetylene. *J. Catal.* **2009**, *262* (2), 199–205. https://doi.org/10.1016/j.jcat.2008.12.011.

(126) Quiroz, J.; Barbosa, E. C. M.; Araujo, T. P.; Fiorio, J. L.; Wang, Y. C.; Zou, Y. C.; Mou, T.; Alves, T. V.; De Oliveira, D. C.; Wang, B.; Haigh, S. J.; Rossi, L. M.; Camargo, P. H. C. Controlling Reaction Selectivity over Hybrid Plasmonic Nanocatalysts. *Nano Lett.* **2018**, *18* (11), 7289–7297. https://doi.org/10.1021/acs.nanolett.8b03499.

(127) Rodrigues, T. S.; Da Silva, A. H. M.; Da Silva, A. G. M.; Ceara, D. G.; Gomes, J. F.; Assaf, J. M.; Camargo, P. H. C. Hollow AgPt/SiO2 Nanomaterials with Controlled Surface Morphologies: Is the Number of Pt Surface Atoms Imperative to Optimize Catalytic Performances? *Catal. Sci. Technol.* **2016**, *6* (7), 2162–2170. https://doi.org/10.1039/c5cy01415h.

(128) Peiris, E.; Hanauer, S.; Knapas, K.; Camargo, P. H. C. Preparation of Silver-Palladium Alloyed Nanoparticles for Plasmonic Catalysis under Visible-Light Illumination. *J. Vis. Exp.* **2020**, *2020* (162), 1–14. https://doi.org/10.3791/61712.

(129) Guler, U.; Suslov, S.; Kildishev, A. V; Boltasseva, A.; Shalaev, V. M. Colloidal Plasmonic Titanium Nitride Nanoparticles: Properties and Applications. *Nanophotonics* **2015**, *4* (1), 269–276. https://doi.org/10.1515/nanoph-2015-0017.

(130) Berrospe Rodriguez, C.; Alvarez Barragan, A.; Nava, G.; Exarhos, S.; Mangolini, L. Stabilizing the Plasmonic Response of Titanium Nitride Nanocrystals with a Silicon Oxynitride Shell: Implications for Refractory Optical Materials. *ACS Appl. Nano Mater.* **2020**, *3* (5), 4504–4511. https://doi.org/10.1021/acsanm.0c00585.

Appendix

Figure A.

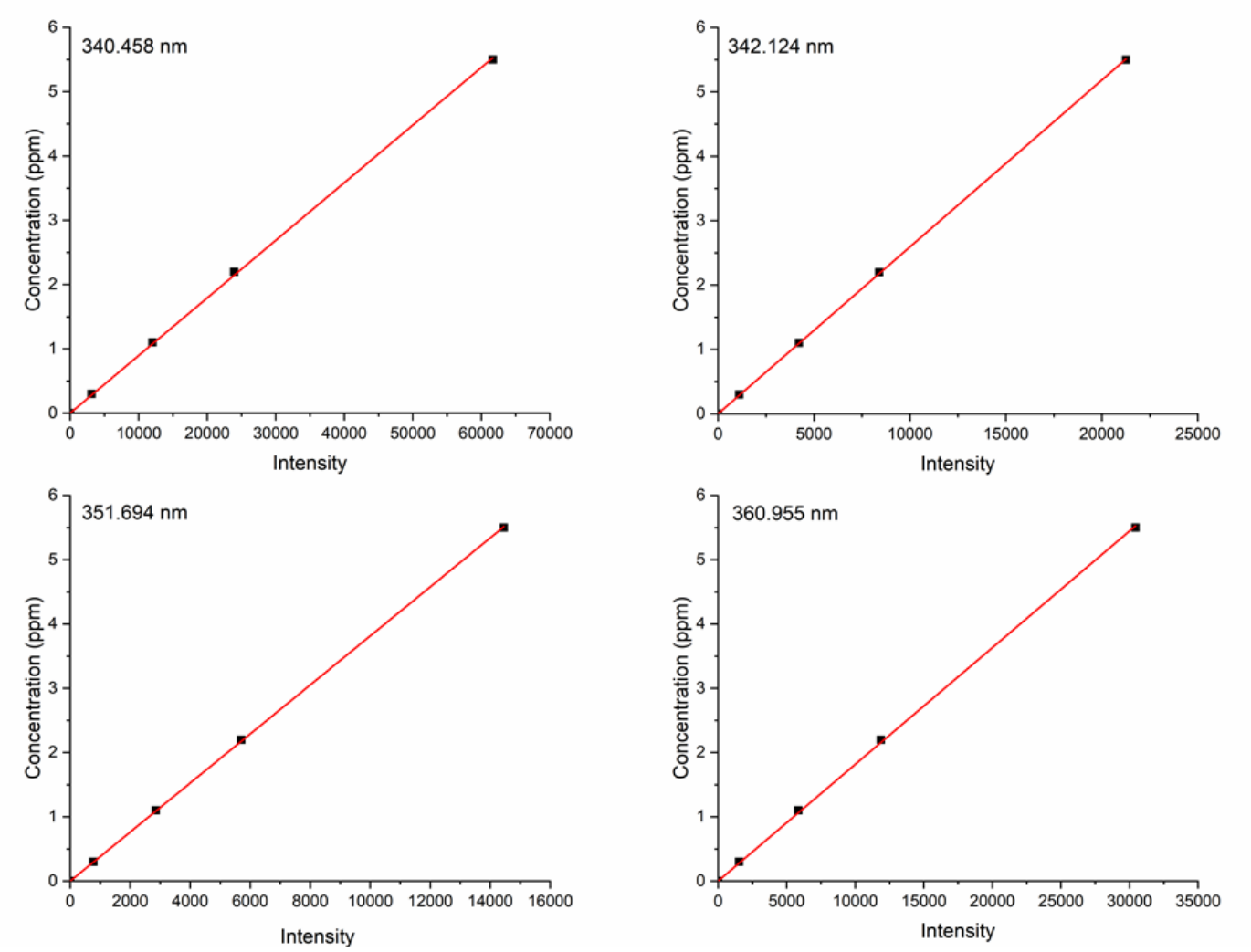

Figure A. Calibration curves for MP-AES analysis of 3 % Pd/TiN (50 nm).

Table A.

Table A. Data for MP-AES analysis of 3 % Pd/TiN (50 nm), two replicate samples

	wavelength of studied emission line (nm)				
Intensities	340.458	342.124	351.694	360.955	
Blank	0	0	0	0	
Standard 1	-	-	-	-	
Standard 2	3147.2	1109.85	773.91	1536.37	
Standard 3	12026.58	4217.76	2854.75	5854.43	
Standard 4	23929.34	8393.44	5700.86	11873.72	
Standard 5	61700.76	21263.07	14455.05	30437.71	
PdTiN 1	23142.24	8102.04	5575.69	11116.85	
PdTiN2	32353.26	11610.59	7948.05	15863.67	
Slope	8.95808E-05	0.000259	0.000381	0.000182	
concentrations (ppm)					Average
Pd/TiN 1	2.073100373	2.100122	2.12639	2.01812	2.08
Pd/TiN2	2.898230913	3.009569	3.031132	2.879843	2.95

Table B

Table B. Reactions for optimisation of phenylacetylene hydrogenation in dark

Pd loading (wt-%)	reaction time (h)	c(PA)(M)	catalyst mass (mg)	T (°C)	Conversion (%)	Selectivity, Ethylbenzene (%)	Selectivity, Styrene (%)
0	20	0.1	30	60	-	-	-
3	20	0.1	30	60	100	100	-
3	4	0.1	30	60	100	100	-
3	4	0.1	30	40	100	100	-
3	4	0.1	30	RT	100	100	-
3	4	0.1	10	RT	100	100	-
0.5	4	0.1	10	RT	100	100	-
0.5	1	0.1	10	RT	82	2	98
0.5	1	0.1	5	RT	98	6	94
0.5	1	0.1	5	RT	89	12	88
0.5	1	0.2	5	RT	52	2	98
0.05	1	0.1	5	40	7	3	97
0.01	2	0.1	10	45	-	-	-

Table C

Table C. Phenylacetylene hydrogenation reactions.

RT: Room temperature

Time (h)	Catalyst mass (mg)	T (°C)	Light/Dark	Conversion (%)	Selectivity, Ethylbenzene (%)	Selectivity Styrene (%)
1	5	RT, heated	L	13	2	98
1	5	40	D	7	3	97
2	5	RT, heated	L	20	2	98
2	5	45	D	21	2	98
1	10	RT, heated	L	22	2	98
1	10	40	D	25	2	98
1	10	RT, heated	L	19	2	98
1	10	40	D	21	2	98
1	10	RT, heated	L	39	2	98
1	10	35	D	10	2	98
1	10	RT, heated	L	63	3	97
1	10	35.0	D	24	57	43
1	10	RT, heated	L	54	3	97
1	10	35.0	D	12	2	98
3	10	RT, heated	L	93	5	95
3	10	35.0	D	80	4	96
3	10	RT, heated	L	89	5	95
3	10	40	D	91	5	95